Hardware-based Complex Natural Resonances extraction techniques for Portable Ground Penetrating Radar devices

Andrés Junior Gallego Garcés

Universidad Nacional de Colombia
Facultad de Ingeniería, Departamento de Ingeniería Eléctrica y Electrónica
Bogotá D.C., Colombia
2022

Hardware-based Complex Natural Resonances extraction techniques for Portable Ground Penetrating Radar devices

Andrés Junior Gallego Garcés

Thesis submitted for the degree of:
Doctor in Electrical Engineering

Advisor:
Ph.D. Francisco Román

Research group:
Electromagnetic Compatibility (EMC-UN)

Universidad Nacional de Colombia
Facultad de Ingeniería, Departamento de Ingeniería Eléctrica y Electrónica
Bogotá D.C., Colombia
2022

Acknowledgements

First of all, I want to thank my advisor, professor Francisco Román, for giving me the strength and the motivation necessary to finish this thesis, for his guidance throughout this process, for introducing me to the scientific world and for all the knowledge he kindly shared with me.

Thanks to all the members of the EMC-UN research group. Without their knowledge and help, this work would have never finished. Specially Edwin Pineda, who dedicated a lot of experimental time to this thesis. To my friends and family, who have always supported me.

Abstract

Here, a contribution to the Improvised Explosive Devices remote detection in Colombia in terms of Ground Penetrating Radar signal analysis is presented. The Complex Natural Resonances Extraction Methods for characterizing buried objects are compared, and from this evaluation and analysis, a new method is proposed with an increased accuracy and hardware suitability factor. Finally, a hardware implementation of this method is tested in an ARM processor.

Keywords: Singularity Expansion Method, Cauchy, Singular Value Decomposition, Linear Prediction Matrix, Vector Fitting, Ground Penetrating Radar, Improvised Explosive Device, Landmine, ARM, processor, Complex Natural Resonances, Poles, Residues, Signal Processing

Abstract

Título: Técnicas basadas en Hardware de extracción de Resonancias Naturales Complejas para operaciones de Radar de Penetración Terrestre

En este libro se presenta una contribución a la detección remota de minas antipersonales en Colombia, en términos del análisis de señales de radar de penetración terrestre. Los métodos de extracción de resonancias naturales complejas para la caracterización de objetos enterrados son comparados, y a partir de esta evaluación y análisis, un nuevo método que muestra un aumento en la presición y en la implementabilidad en *hardware* es propuesto. Finalmente, este método es implementado en un procesador ARM.

Palabras clave: Método de expansión de singularidades, Cauchy, Descomposición en Valores Singulares, Matriz de Predicción Lineal, Ajuste de Vectores, Radar de Penetración Terrestre, Dispositivos Explosivos Improvisados, Minas Antipersonales, Procesador ARM, Resonancias Naturales Complejas, Polos, Residuos, Procesamiento de Señales.

List of figures

List of tables

Glossary

ARM Advanced Risk Machine processor brand.

CNN Convolutional Neural Network.

CNR Complex Natural Resonances.

CNREM Complex Natural Resonances Extraction Method.

FPGA Field Programmable Gate Array.

FSV Feature Selective Validation.

GPR Ground Penetrating Radar.

H Transfer Function in frequency domain.

HW platform Hardware Platform.

IED Improvised Explosive Device.

LP Linear Prediction matrix.

LTI Linear Time Invariant system.

MD Metal Detector.

MPM Matrix Pecil Method.

SEM Singularity Expansion Method.

SVD Singular Value Decomposition.

VCM Vector Fitting Cauchy Method.

VF Vector Fitting.

Contents

1. Introduction

Improvised Explosive Devices (IEDs), also called Unexploded Ordnance (UXO), have been deployed around the world for decades and yet, due to the lack of standarization in the manufacturing processes, many soil compositions, explosive types, disposal process, and even the triggering mechanism, they remain buried and active for many years. This has resulted in thousands of civil casualties and injuries in almost every country where a conflict has existed [9].

According to government statistics, Colombia was the country with more casualties after Afganistan due to improvised landmines in 2017, which are still being deployed on a daily basis because of an internal war [10]. The most updated statistics estimate 12.152 landmines victims, where 40% corresponds to civil unarmed persons, mostly children. In January 2022, 6 new victims were reported in Colombia again [11].

When it comes to IEDs extraction process for humanitarian purposes, a non-invasive localization and detection methods become necessary, currently carried on by metal detectors (MD). However, this process is slow and expensive, beside the always present risk for the MD operator. On the other had we have Ground Penetrating Radar techniques, such as the Singularity Expansion Method (SEM) and the theory that it can classify buried objects no matter its orientation based on the Complex Natural Resonances (CNR) calculated from the backscattering response. To classify buried objects in real time based on SEM will help the demining procedure for IEDs and the possibility of training and learning, saving possibly thousands of lives. The selection, improvement and implementation of an algorithm that classifies objects in operation time is the aim of this thesis, leading to a low-cost portable and efficient improvised landmine detector device that could be easily manufactured and deployed in civil ground.

1.1. Objectives

The main objective of this thesis is to design a hardware-based algorithm for complex natural resonances extraction techniques in portable ground penetrating radar devices.

- To compare and select complex natural resonances extraction methods based on computational cost, accuracy and overall suitability for hardware implementation.

- To increase the efficiency of CNR extraction techniques for a hardware implementation.
- To design and test a version of the developed algorithm for the extraction of CNRs .

1.2. Outline

This document is organized as follows: first, the Radar and Ground Penetrating Radar signal acquisition process is explained in Chapter 2, then the Complex Natural Resonances Extraction Methods (CNREM) explanation and automation is showed in Chapter 3, leading to the performance comparison and analysis in Chapter 4. The proposed method improving key aspects of CNREM is presented in Chapter 5, while the hardware algorithm implementation is presented in Chapter 6. Finally, the conclusions, future work and appendixes are included.In appendix A, a method for the input Linear Prediction matrix segmentation is proposed, Appendix B shows an study on data compression with SEM, while in Appendix C a channel identification and modeling of two antennas based on SEM are presented.

1.3. Contribution

- Study of low-cost GPR radar techniques for buried object detection, and adaptation of the multilayered medium transfer function modeling for landmine detonators detection.
- CNREM automation for principal resonances filtering.
- Reconstruction and resonance validation of CNREM with R^2 and FSV methods.
- SEM algorithms comparison and performance evaluation.
- Proposed Hardware suitability factor equation for CNR extraction methods.
- New method improving accuracy and Hardware suitability factor of CNREM, based on the insights of coming from the comparison.
- Hardware-based design for the ARM Cortes-A9 processor.
- Parallelization and LP matrix segmentation for hardware and efficiency purposes based on SEM
- Data compression with SEM

- Channel identification and modeling of two antennas based on SEM

2. Radar signal acquisition and pre-processing

2.1. Ground Penetrating Radar

Ground Penetrating Radar (GPR) is a non-invasive measurement technique where radio waves illuminate the soil, and then the reflected or backscattered signal provides information to image the subsurface, leading to the presence of static targets or the determination of media changes. The signal measurement in a basic scheme, as displayed in Figs. **2-1** and **2-2**, compares field amplitude versus time after excitation. This is usually done in time-domain, however, frequency domain methods are also being used to complete this task [1].

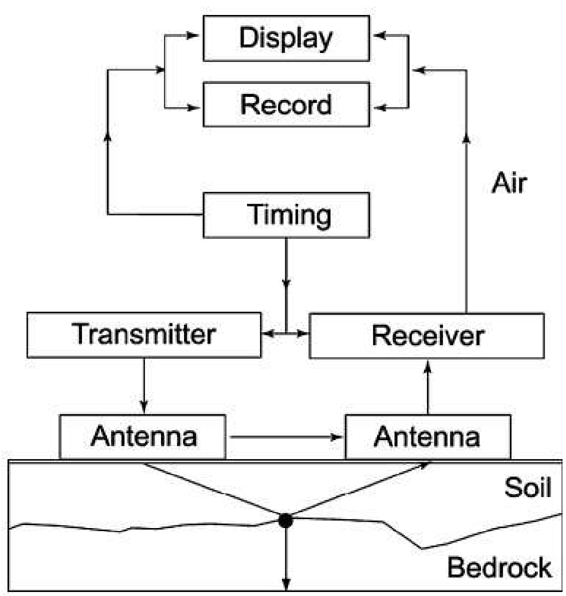

Figure **2-1**.: Main components of a ground penetrating radar device [1].

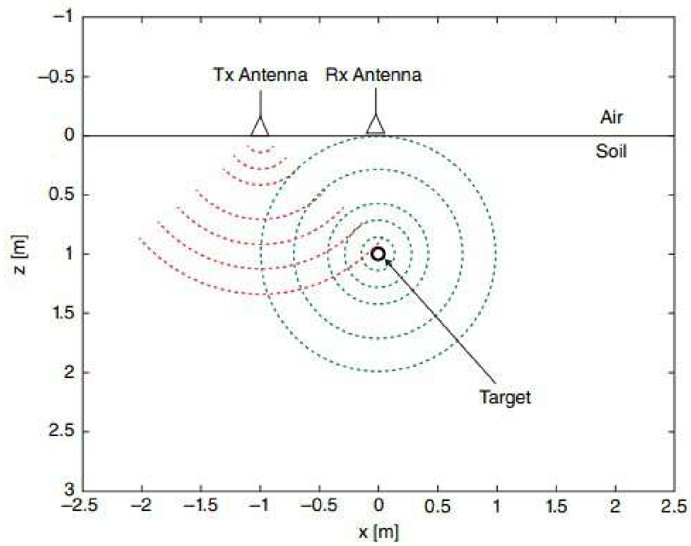

Figure **2-2**.: Working principle of GPR backscattering system. [2].

As a non-destructive tool for mapping a subsurface, some of the areas where GPR has been used are:

- Archaeology, by testing and identifying numerous unmarked burials in a rock shelter using a geographic information system [12].
- Structures and pavements, widely used as a way of locating buried structures, determining soil composition, and detecting underground water and ice [13].
- Military and humanitarian applications, as GPR can be used to detect hidden bunkers and tunnels [14].
- Medicine, for monitoring the deployment of arterial stents [15].
- Studies for cemetery and criminal investigations [16]

Demining is another application of interest. Even though metal detectors determine the presence of metal, a GPR can possibly determine the position, the size and the shape of the target. Some particular advances in this area have been presented with a hand-held GPR in [17].

Some of the most common technologies used nowadays are impulse radar, continuous-wave, ultra-wide band, and synthetic-aperture radar, even from a few MHz to the VHF or UHF bands.

Moreover, algorithms needed for image generation could be classified as clutter suppression (define the background model and then subtract it from the measured signal), focusing (use a radon transformation to coherently sum the signals scattered by localized objects) and feature based target detection (hypothesis testing theory including the target signature and the clutter) [18, 19].

2.2. Radar signal acquisition and pre-processing

The low-cost radar measurement setups for time and frequency domain signal generation and acquisition consisted in a portable Vector Network Analyzer (VNA) and two Vivaldi antennas for ground penetrating and free space configurations as Fig. **2-3** shows. Here, the media was air for open space, and sand or soil for the GPR measurements.
A miniVNA Tiny Plus 2 up to 3 GHz was used to obtain the S21 parameters for every open-space metallic objects experiments, with 1000 steps for the frequency range. For measurements of buried objects, a R&S ZVH VNA was used up to 6 GHz and 1001 samples for the complete bandwidth. Although the signal was captured using the whole spectrum, the resonances calculated in the following chapters considered only frequencies above 600 MHz.

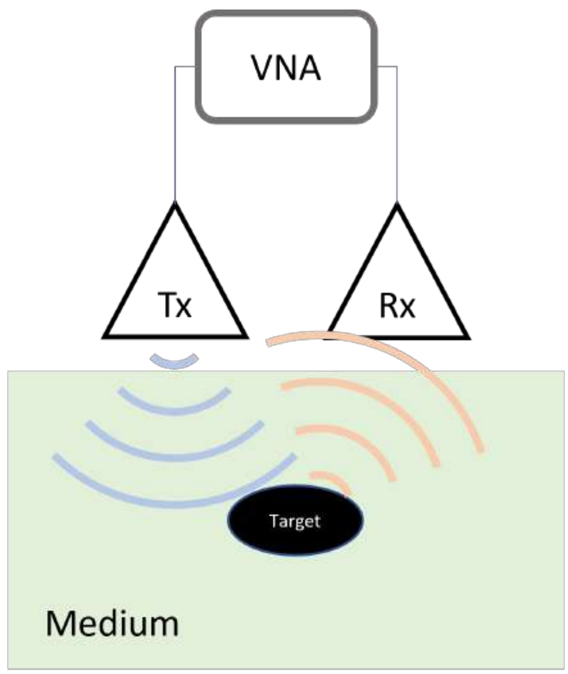

Figure **2-3**.: Basic Radar system configuration for free space and ground penetrating configurations.

The antennas used were two RFSpace TSA600, showed in Fig. **2-4**, that provided the frequency range, gain and low VSWR as in Fig. **2-5** over the full range for minimizing resonances in a low-cost setup [3]. After the signals were acquired, the post-processing was achieved in an Core i7 PC running Software like Matlab and some of the Vivado suite for the hardware-based algorithm design and comparison.

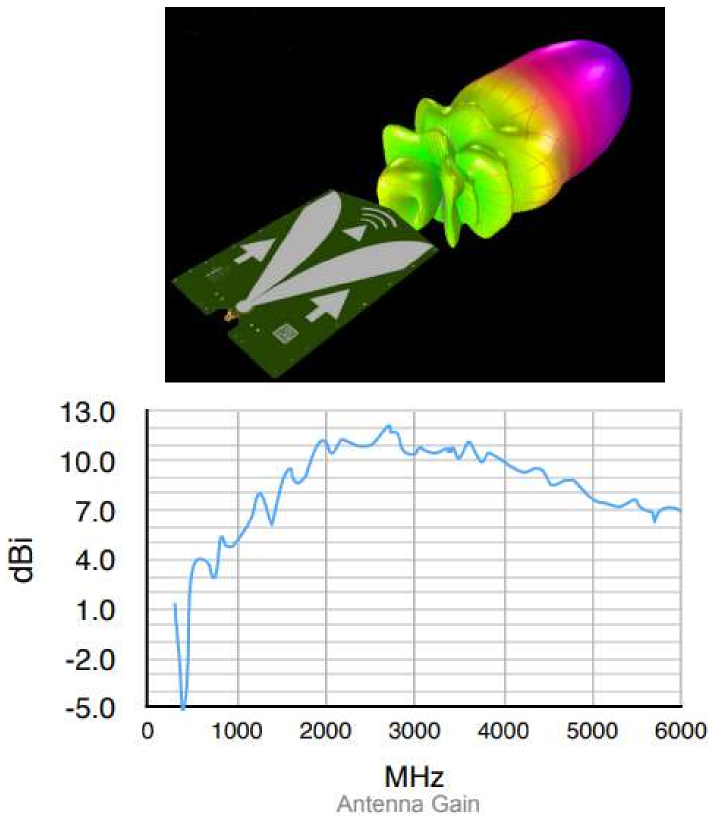

Figure **2-4**.: RFSpace TSA600 Ultra-Wideband PCB Tapered Slot Antenna [3].

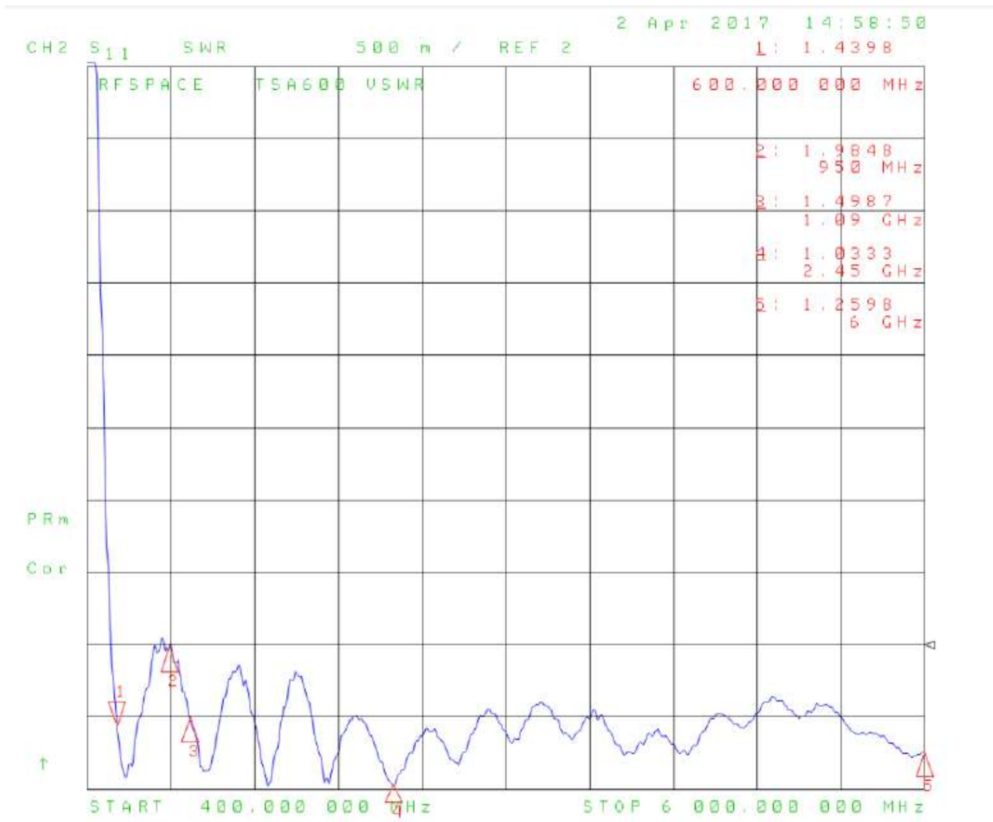

Figure **2-5**.: Vivaldi PCB antenna TSA600 VSWR from 400 MHz to 6 GHz [3].

For the signal pre-processing, the measurements were considered as a Linear Time-Invariant (LTI) Impulse Response (IR) [20, 21]. Eqs. 2-1 and 2-2 describe the system response for time and frequency domains

$$y(t) = x(t) * h(t) \rightarrow y(t) = \delta(t) * h(t) \rightarrow y(t) = h(t) \quad , \tag{2-1}$$

and

$$Y(j\omega) = X(j\omega)H(j\omega) \rightarrow Y(j\omega) = H(j\omega) \rightarrow Y(j\omega) = H(j\omega) \quad , \tag{2-2}$$

- $y(t)$: time domain output signal
- $x(t)$: time domain input signal
- $h(t)$: time domain system response
- $*$: convolution operator
- $Y(j\omega)$: frequency domain output signal
- $X(j\omega)$: frequency domain input signal

- $H(j\omega)$: frequency domain system response

For this reason, using Dirac impulses as the input signal implies that the output signal is equal to the system response. Moreover, undesirable returns as antenna coupling crosstalk, antennas unexpected behavior, surface reflections, background and objects reflections other than the target can be considered as clutter and expressed as in Eq. 2-3, with $H_c(j\omega)$ and $H_t(j\omega)$ as the clutter and target impulse responses [22].

$$Y(j\omega) = X(j\omega)[H_c(j\omega) + H_t(j\omega)] \tag{2-3}$$

Reducing the clutter response is considered here as a background removal, different than the common for B-scan and C-scans [2]. Instead of dealing with the average of the background and filters, the bistatic radar system used the VNA-antenna-medium system modeling proposed by Lambot et. al. [4, 23, 24]. Although the model is proposed for a monostatic setup, it has been adapted for this pre-processing.
The return loss transfer function $A_i(j\omega)$, the transmitting and receiving transfer functions $A_t(j\omega)$ and $A_r(j\omega)$ of the antenna, and the multilayered medium system reflections $A_f(j\omega)$, incorporate the clutter in the transfer function system response as in Fig. **2-6**. In other words, $A_i(j\omega)$, $A_t(j\omega)$, $A_r(j\omega)$ and $A_f(j\omega)$ are comprehended in $H_c(j\omega)$, adding noise to the signal of interest $H_t(j\omega)$.

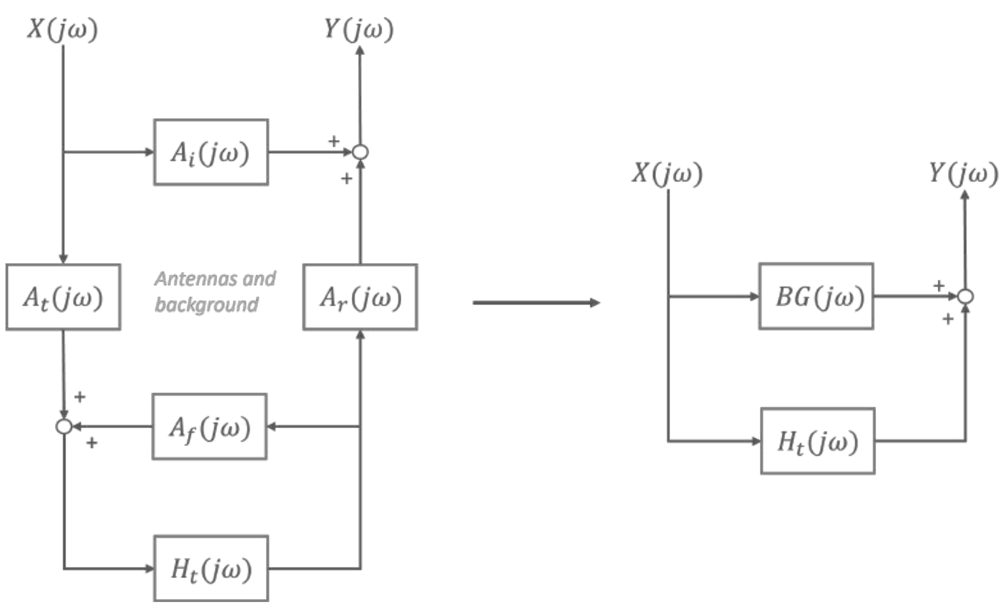

Figure **2-6**.: Multilayered medium transfer function modeling proposed in [4], and adaptation for the bistatic basic measurement setup.

This leads to Eq. 2.2 where transfer function $H_c(j\omega)$ is considered as background, and the parameter S_{21} can be found.

$$S_{21} = \frac{Y(j\omega)}{X(j\omega)} = BG(j\omega) + H_t(j\omega) \tag{2-4}$$

As $BG(j\omega)$ can be measured directly by performing measurements in free space conditions or in the setup without target, then the transfer function of interest $H_t(j\omega) = S_{21} - BG(j\omega)$ can be obtained from the backscattered signals.

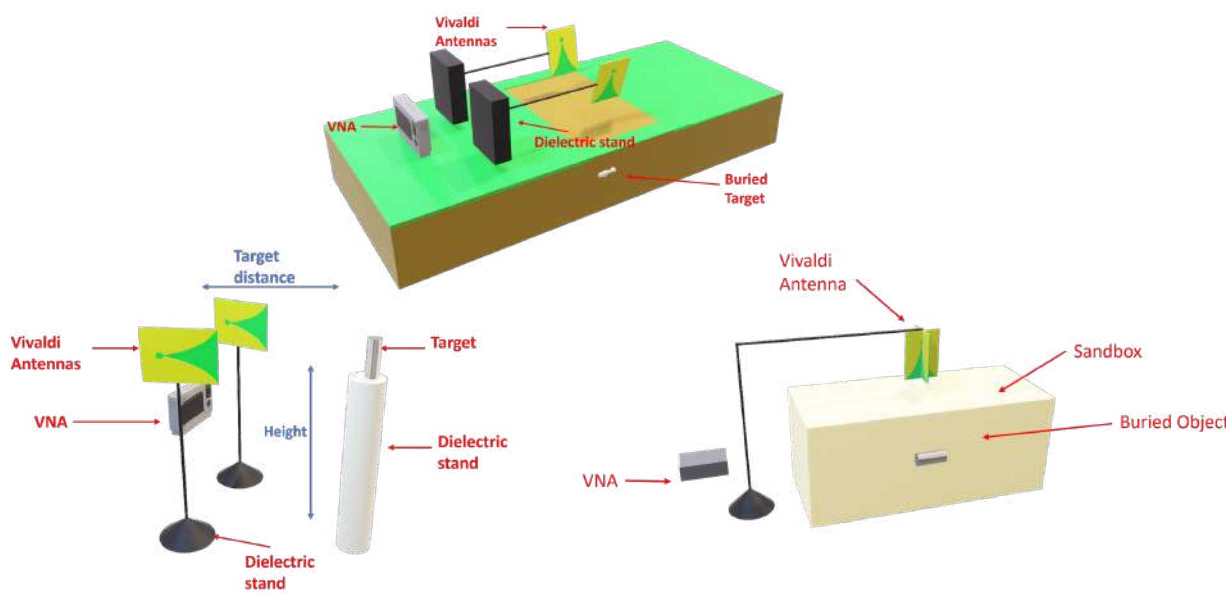

Figure **2-7**.: Experimental setups in soil, free space and sandbox for signal generation and retrieval.

For all the scenarios, the antennas and the target were separated more than 0.4 m for every of the three setups shown in Figs. **2-7** and **2-8**, where the signal acquisition was achieved, then pre-processed with the previous modeling, and then used as an input for the Complex Natural Resonances Extraction Methods (CNREM).

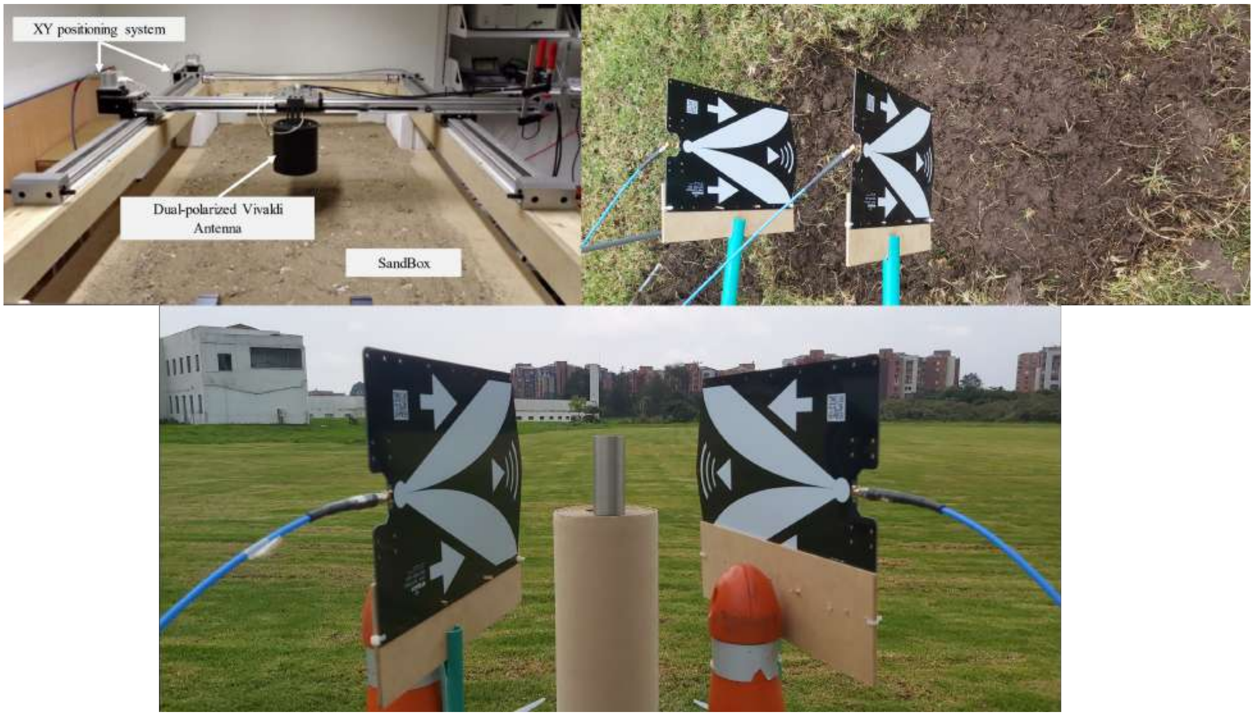

Figure **2-8**.: Antennas and backscattering objects, including the sandbox experiments carried out in Germany by S. Gutierrez [5].

3. Complex Natural Resonances Extraction Methods

The Complex Natural Resonances Extraction Methods (CNREM) derived from the Singularity Expansion Method (SEM), are able to decompose a time or a frequency domain signal in a set of frequency components and damping factors, called Natural Resonances. In this chapter, we will first review the overall SEM background before going in the direction of Cauchy, Matrix Pencil Method and Prony's Methods. After this, the critical components of each method are analyzed in order to identify possible improvement aspects for real-time operations or accuracy increase in backscattering scenarios [25].

3.1. Complex Natural Resonances

The relationship between the material and shape of an object with the natural electromagnetic frequencies or resonances was introduced two times. One by Kennaugh, Moffat and Mains since 1965 and then by C. Baum in 1971 [26, 27] [28]. Although the inspiration and methodology is slightly different, they both implied pure frequencies unique for a combination of shape and material (object) from the backscattered response after being illuminated with an EM wave.

After this, the development of methods for calculating these natural resonances or frequencies of objects appeared. For the most part, analytical solutions include integral equations and approximate methods for the extraction of natural frequencies of straight wire antennas and simple shaped scatterers [29–33].

In this context, the rational functions approximations take place, even used as a SEM approach to calculate the resonances of buried objects. Prony's, Cauchy's and Matrix Pencil methods are part of this, starting with the linear prediction matrix and then calculating the approximated Complex Natural Resonances.

3.2. Singularity Expansion Method (SEM)

Carl Baum in 1971 developed SEM theory inspired by the backscattering transient responses observable in various experiments, where a few damped sinusoids appeared to be the main dominating components of the waveform from complicated aricraft scatterers [28, 34]. As the idea of expanding the response of damped sinusoids for EMP experimental observations in terms of all the singularities in the complex frequency plane, this has became a backscattering signal identification method, mainly because the pole locations do not depend on the orientation of an object. This CNR signature for an object illuminated with an EM wave is unique, and has been used in time and frequency domain signals for CNRs (or poles) extraction [35–37].

The general SEM equation proposed by Carl Baum is in 3-1, where the input signal $y(t)$ is approximated according to the sum of damped exponentials. R_n are the complex residues or amplitudes, and s_i are the CNRs or poles from which the input signal can be reconstructed from.

$$y(t) \approx \sum_{i=1}^{M} R_n e^{-s_i t} \tag{3-1}$$

After this mathematical representation of a signal, then the evidence of its singularities is shown as complex numbers associated to damped sinusoids. Notice how $s_i = \alpha_i + j\omega_i$, meaning that the set of poles is based on damped sinusoids (as long as the resonances are located in the left side of the complex plane) with ω_i as the resonant frequencies. These singularities can be considered an electromagnetic signature of the object and be calculated through several SEM based methods: the Matrix Pencil Method, TLS-Prony's Method and Cauchy's Method, in frequency or time domain [38–40].

Ground Penetrating Radar signal processing by Moffat and Mains proposed in 1975 the use of SEM for aircraft identification, and only four years later, L.C. Chan used higher frequencies and successfully identified that the CNRs of a plastic landmine did not change after leaving it buried for a year. The soil parameters did change, but the resonances remained the same [41]. The CNRs of the mine were independent of the electrical parameters of the medium [42].

In [43], D.V Giri and Frederick M. Tesche described alternative analytical methods for determining the natural frequencies of a thin wire with a diameter to length ratio below 0.005, and mention SEM as an useful method for more complex structures like the ones treated here. In Ground Penetrating Radar (GPR) operations, for example, the idea is to use these methods in order to identify a buried object.

This chapter has an overview of MPM, Prony and Cauchy methods, the mathematical outline for the algorithm construction, benchmark, simulation and experimental examples for calculating CNRs in some backscattering scenarios.

3.3. TLS-Prony's

This can be chronologically considered as the first time domain method for computing the SEM CNRs of a backscattered signal in time domain, and it is based on the 1795 Prony's method for solving a non-linear problem using a linear prediction equation with an unknown coefficient vector. The relatively recent updates on this method have increased the Signal to Noise Ratio (SNR) tolerance for SEM, and were able to calculate complex poles and residues from a signal using computer software [39, 44].

TLS-Prony's method starts with the linear prediction equation in 3-2, which is similar to SEM but takes into account the associated noise W_n. This has c_m and S_m as the amplitudes and complex resonances up to P for N number of samples,

$$y_n \approx \sum_{i=1}^{P} c_m e^{nS_m t} + W_n, \quad n = 0, 1, ..., N-1. \tag{3-2}$$

Afterwards, an LP matrix in the form of $Ab \approx g$ can be constructed from the sampled signal. The linear predictor and the observation vector can be treated as if we were searching for the solution vector in the form of minimizing the l_2 norm for g [45–47]. Equation 3-3 shows the parameter L as an overestimate of the number of complex exponentials to be computed from the data and b_m as the polynomial coefficients from which the poles are calculated with $b_0 = 1$.

$$\begin{bmatrix} y_{L-1} & y_{L-2} & \cdots & y_0 \\ y_L & y_{L-1} & \cdots & y_1 \\ \vdots & \vdots & \ddots & \vdots \\ y_{N-2} & y_{N-3} & \cdots & y_{N-L-1} \end{bmatrix} \begin{bmatrix} b_0 \\ b_1 \\ \vdots \\ b_{m-1} \end{bmatrix} = \begin{bmatrix} y_L \\ y_{L+1} \\ \vdots \\ y_{N-1} \end{bmatrix} \tag{3-3}$$

Parameter L is critical for the linear predictor method, because if this number is not close to the number of CNRs, spurious poles appear in the complex plane. As the response approximation is based on the sum of the poles and the associated residues, then all the resonances are contaminated and not accurate. In order to minimize this, the noise vectors E and r are added to A and g respectively as in equations 3-4, 3-5 and 3-6.

$$(\mathbf{A} + \mathbf{E})\mathbf{b} = \mathbf{g} + \mathbf{r} \quad , \tag{3-4}$$

which leads to

$$[(\mathbf{A}|\mathbf{g}) + (\mathbf{E}|\mathbf{r})]\frac{\mathbf{b}}{-1} = 0 \quad , \tag{3-5}$$

and

$$(\mathbf{B} + \mathbf{D})\mathbf{z} = 0 \quad . \tag{3-6}$$

This is where the SVD decomposes the matrix B for a rank fix, where only the principal eigenvalues determine the L parameter minimum for an unique solution. Then, a TLS is used for solving the linear system in 3-2 and find the solution vector b.

Looking at the method in a general way as in Figure **3-1** provides the first insight for matrix calculations: the dependance on SVD for eigenvalues extraction (which are directly related to the resonances) [39].

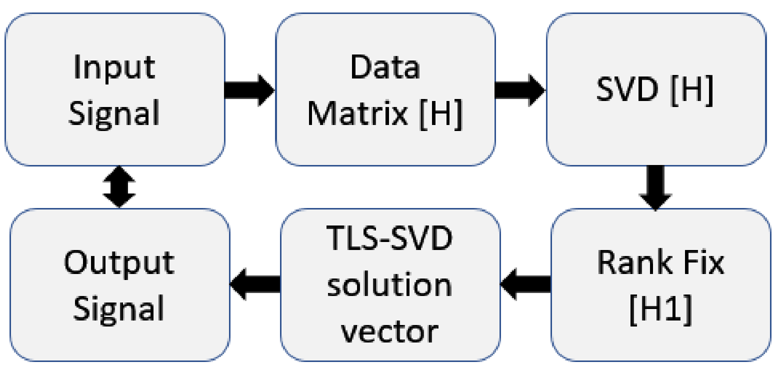

Figure **3-1**.: General step by step TLS-Prony's Method with $[H]$ as the input data matrix

A simple test with the benchmark signal $y(t) = \sin(8t) + \sin(12t)$ is done here to show the poles calculation and the validation of these through the reconstruction of the input data. Figure **3-2** has hte input data and the corresponding reconstruction, while figure **3-3** displays the CNRs.

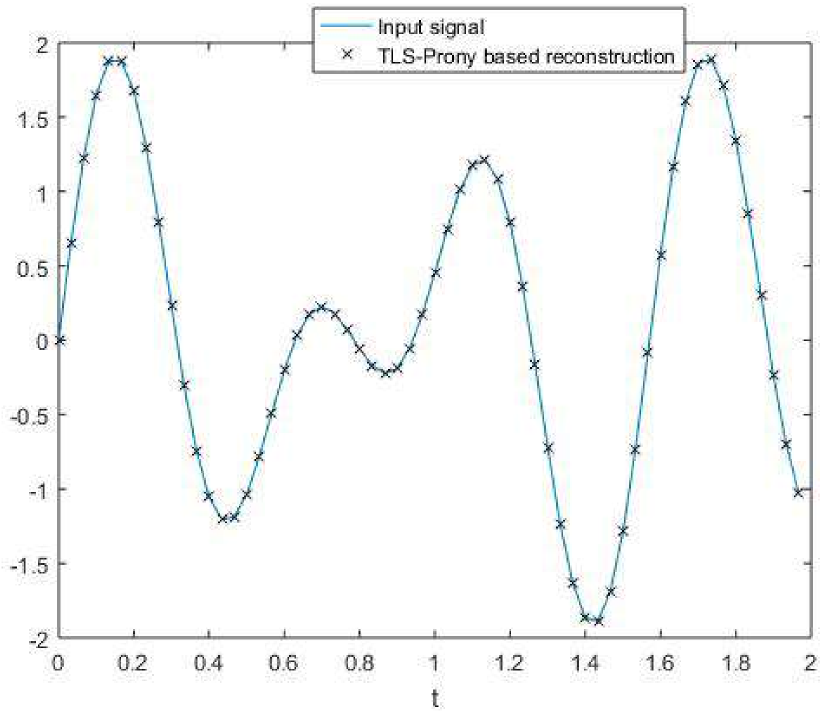

Figure **3-2**.: Benchmark signal with resonances at 12 and 8, and Prony-based reconstruction.

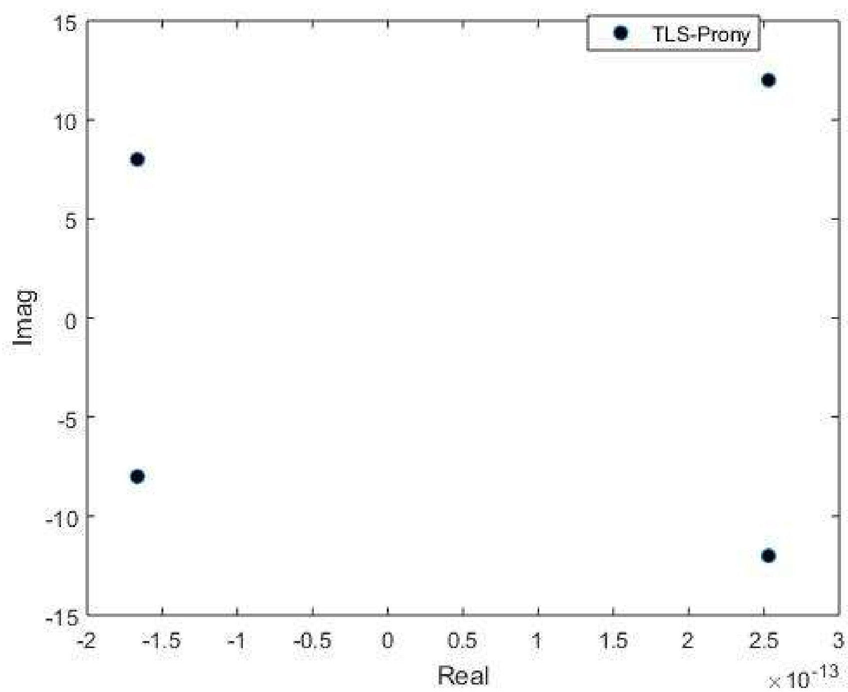

Figure **3-3**.: Prony's calculated CNRs for a benchmark signal with resonances at 12 and 8.

See how the poles come in conjugate pairs and represent frequencies 8 and 12 (the same as in the input signal). Also, as this is not a finite decaying signal, some resonances appear in the right part of the complex plane with positive real values. The resonances for backscattering signals should appear in the left side of the complex plane.

3.4. Matrix Pencil Method

After Prony's approach and the TLS solution improvement to increase the noise tolerance of the results, then Hua and Sarkar proposed an alternative method in 1990. Based in the Pencil of Function (PoF), the solution to the SEM equation, i.e. the poles and residues of the time domain input signal, could be found from a Hankel matrix and two or more SVDs [38, 48, 49]. This method has been used to extract the characteristics of time domain signals in EM backscattering scenarios for the evaluation of geological formations and underwater sound signal identification, among others [50, 51].

Again, the time-domain SEM equation in discrete form 3-7 is the starting point, with:

- y_k: sampled input signal in time domain
- M: number of CNRs of the approximated signal
- $z_n = e^{s_n T_s}$: complex exponentials basis
- T_s: sampling period
- R_n residues

$$y_k \approx \sum_{n=1}^{M} R_n z_n^k \tag{3-7}$$

For the linear predictor, a Hankel matrix is constructed from 3-7 as in 3-8, having the first estimate of the pencil parameter L as $N/2$ or $N/3$, being N the number of samples. This is used to balance the computational accuracy and cost, as the following matrix operations directly depend on the matrix size. There have been studies analyzing the balance between computational cost and accuracy as in [52].

$$Y = \begin{bmatrix} y_o & y_1 & \cdots & y_L \\ y_1 & y_2 & \cdots & y_{L+1} \\ \vdots & \vdots & \ddots & \vdots \\ y_{K-L-1} & y_{K-L} & \cdots & y_{K-1} \end{bmatrix} \tag{3-8}$$

To find the principal components of this LP matrix, equation 3-9 is used with λ values, i.e. the principal components of the matrix, that make the singular solution equal to 0. Here, H is the Hermitian transpose of a matrix, and has $[Y_1]$ and $[Y_2]$ as the matrix $[Y]$ with the last and the first column deleted respectively. This singular solution is equivalent to 3-10, where the superscript + denotes the matrix pseudo-inverse.

$$[Y_2]^H - \lambda[Y_1]^H \tag{3-9}$$

$$\lambda = [Y_1^H]^+[Y_2^H] \tag{3-10}$$

Now, before the full Hankel matrix inversion, the Singular Value Decomposition $[Y] = [U][S][V]^H$ comes in handy to reduce noise and computational cost. T is the general transpose of a matrix, $[U]$ has the largest n orthonormalized eigenvectors of $[Y][Y]^H$, and $[V]$ the eigenvectors from $[Y]^H[Y]$. The singular values composing S are the non-negative square roots of the eigenvalues of $[Y]^H[Y]$. After this matrix is constructed, and assuming a noisy environment, a new matrix $[Y']$ and its corresponding $[U']$, $[S']$ and $[V']$ could be defined, setting a minimum threshold in order to delete the non-zero and noise dependent eigenvalues in $[Y]$.

The selection of this threshold is based on p, the number of significant decimal digits in the input data signal as in equation 3-11. The ratio between the σ_M diagonal value of $[S]$ and the maximum σ_{max} allows the selection of M principal components so that the $[Y']$ matrix can be formed. In other words, this new matrix has a rank fix and reduced number of elements, lowering the straighforward computational cost and noise associated components.

$$\frac{\sigma_M}{\sigma_{max}} = 10^{-p} \tag{3-11}$$

The previous rank fix for the construction of $[Y']$ leads to $[U']$, $[S']$ and $[V']$, as mentioned before. The solution for the system in 3-9 becomes then $\lambda = [Y_1'^H]^+[Y_2'^H]$. Now, instead of computing the Moore-Penrose pseudo-inverse directly, another SVD is used over $[V']$ in order to find λ as in equation 3-12.

$$\lambda = [V_1'^H]^+[V_2'^H] \tag{3-12}$$

As mentioned before, the pseudo-inverse direct computation is replaced by an SVD based procedure, which consumes less resources. Now, if $[V1]^T = [U_v][S_v][V_v]^H$, then the equation 3-13 computes the pseudo-inverse with the new diagonal matrix $(S_v')_{ii} = 1/(S_v)_{ii}$. That is to say, changing the order and a simple diagonal elements division finds the Moore-Penrose pseudo-inverse with reduced computational effort.

$$[V_1'^H]^+ = [V_v][S_v'][U_v^H] \tag{3-13}$$

So far, the input Hankel matrix has been constructed, rank reduced, and the inverse of the matrix $[V']$ has also been computed. Going back to Eq. 3-12, the solution for λ is:

$$\lambda = [V_1'^H]^+[V_2'^H] = [V_v][S_v'][U_v^H][V_2'^H] \quad , \tag{3-14}$$

which are the poles λ_i of the input signal, transformed into $s_i = \frac{1}{\Delta t}\log(\lambda_i)$ with $i = 1, ..., M$. These s_i are the poles of the general SEM form in 3-1, or the equivalent s_i from z_n from equation 3-7. The residues R_n, on the other hand, are yet to be calculated. The least-square approach allows this calculation starting from a Vandermonde Matrix constructed from the input data and exponential copies of z_n as in Eq. 3-15. This concludes the Matrix Pencil Method, and the general steps are shown in Figure **3-4**.

$$\begin{bmatrix} y_o \\ y_1 \\ \vdots \\ y_{K-1} \end{bmatrix} = \begin{bmatrix} 1 & 1 & \cdots & 1 \\ z_1 & z_2 & \cdots & z_M \\ \vdots & \vdots & \ddots & \vdots \\ z_1^{K-1} & z_2^{K-1} & \cdots & z_M^{K-1} \end{bmatrix} \begin{bmatrix} R_1 \\ R_2 \\ \vdots \\ R_M \end{bmatrix} \tag{3-15}$$

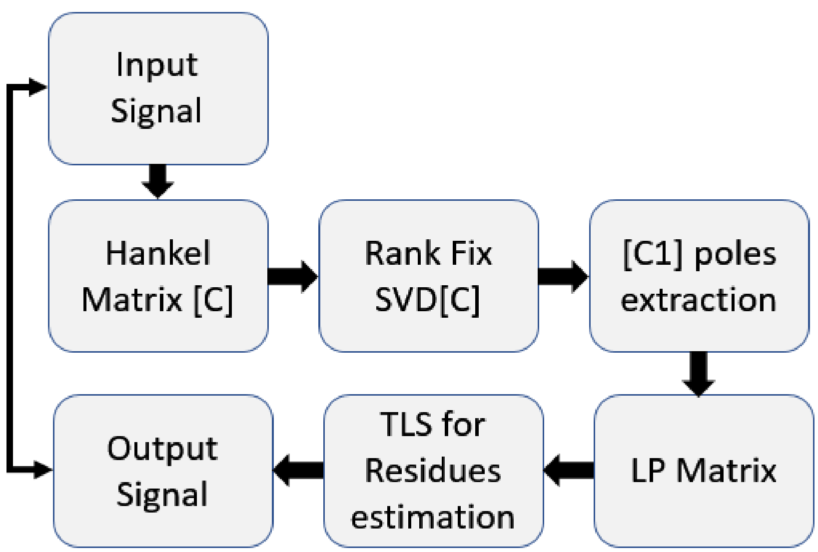

Figure **3-4**.: General step by step MPM with $[C]$ as the input matrix.

One more, a benchmark signal $y(t) = \sin 5t + \sin 10t$ is used as input data to confirm MPM correct functionality. The CNRs should have frequencies 5 and 10, and the reconstruction should be accurate enough. Figures **3-5** and **3-6** display the input data, the reconstruction based in the poles and residues calculated with MPM, and the poles in the complex plane.

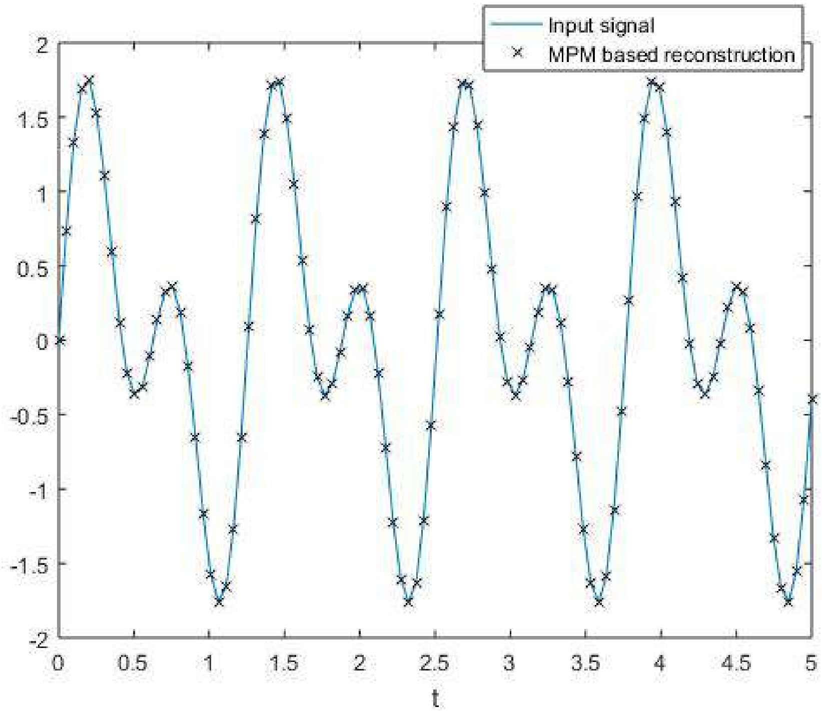

Figure **3-5**.: Benchmark signal $y(t) = \sin 5t + \sin 10t$ and its reconstruction using MPM.

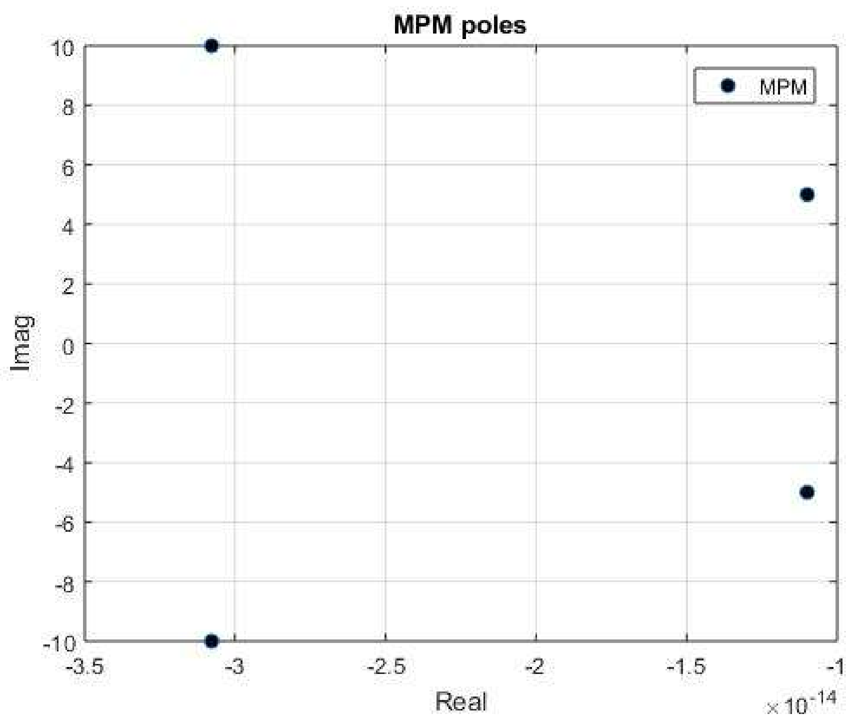

Figure **3-6**.: CNRs calculated with MPM for a benchmark signal $y(t) = \sin 5t + \sin 10t$.

The reconstruction is accurate, and the poles come in conjugate pairs with the frequencies expected. This time, all the resonances are in the left-hand part of the complex plane.

3.5. TLS-Cauchy

As TLS-Prony and MPM calculate the CNRs from a time-domain signal, Cauchy's method approaches frequency-domain signals. It was presented back in 1821, as a ratio of two polynomials approximating a function, also assuming a Linear-Time Invariant (LTI) response as in equation 3-16 [40, 53]. After that, it has been applied to the solution to electromagnetic problems modeling the system frequency response in the same way [54].

$$H(f_i) \approx \frac{A(f_i)}{B(f_i)} = \frac{\sum_{k=0}^{P} a_k f_i^k}{\sum_{k=0}^{Q} b_k f_i^k}, \quad i = 1, 2, \ldots, N \tag{3-16}$$

A Partial Fraction Expansion (PFE) of the numerator and the denominator polynomials $A(f_i)$ and $B(f_i)$ are the residues and poles of the input signal as in equation 3-17, where M is the estimated number of CNR, and again $s_m = \alpha_m + j\omega_m$. Notice how this is the frequency-domain equivalent of the general SEM equation in 3-1.

$$H(f_i) \approx \frac{A(f_i)}{B(f_i)} = \sum_{m=1}^{M} \frac{R_m}{\omega - s_m} \tag{3-17}$$

The system in equation 3-18 is the starting point for the solution of 3-16, where $[C]$ is constructed as in equation 3-19, and $Q = P + 1$ to guarantee the denominator polynomial order higher.

$$\begin{bmatrix} A & -B \end{bmatrix}_{N\times(P+Q+2)} \begin{bmatrix} a \\ b \end{bmatrix}_{(P+Q+2)\times 1} = [C]_{N\prod(P+Q+2)} \begin{bmatrix} a \\ b \end{bmatrix}_{\times(P+Q+2)\times 1} = 0 \tag{3-18}$$

$$[C] = \begin{bmatrix} 1 & f_1 & \cdots & f_1^P & -H_{f_1} & -H_{f_1} f_1 & \cdots & -H_{f_1} f_1^Q \\ 1 & f_2 & \cdots & f_2^P & -H_{f_2} & -H_{f_2} f_2 & \cdots & -H_{f_2} f_2^Q \\ \vdots & \vdots & \ddots & \vdots & \vdots & \ddots & \vdots & \\ 1 & f_N & \cdots & f_N^P & -H_{f_N} & -H_{f_N} f_N & \cdots & -H_{f_N} f_N^Q \end{bmatrix} \tag{3-19}$$

This initial matrix $[C]$ has the frequency elements up to the power of Q, which means that the numerical noise increases with the number of frequency samples and the overall matrix size. Also, as $[C]$ is $N \times (P+Q+2)$, the solution is unique if $N \geq P+Q+2$. Reducing the size of $[C]$ keeping a unique solution is then critical.

The SVD of the input data matrix for a rank fix, estimating the number of principal components, reduces the number of elements. The diagonal singular values of $[S]$ from $[C] = [U][S][V]^H$ are organized in descending order, so, a threshold is applied to this values based in the number of significant decimal digits of the system response data as in equation 3-20. This is the same approach previously shown in MPM,

$$\frac{\sigma_M}{\sigma_{max}} = 10^{-p} \quad , \tag{3-20}$$

and then, the number of non-zero singular values R in $[S]$ after this threshold is $R = P+Q+2$.

The resulting matrix $[C1]$ is rank reduced, and now the system in 3-18 can be solved for a and b using a TLS approach. However, when it was presented as a SEM-like method in 2012, a QR decomposition was proposed for the solution of this system, increasing numerical noise tolerance [40].

This QR decomposition starts with $[A]$ in 3-18 because it is formed with frequency components only, not altered by measurement errors or noise. With $[A] = [Q][R]$, $[C]$ becomes

$$[A \quad -B] = Q^T[A \quad -B] = [Q^TQR \quad -Q^TB] = [R \quad -Q^TB] \quad , \tag{3-21}$$

resulting in the following system

$$[R \quad -Q^TB]\begin{bmatrix} a \\ b \end{bmatrix} = \begin{bmatrix} R_{11} & R_{12} \\ 0 & R_{22} \end{bmatrix}\begin{bmatrix} a \\ b \end{bmatrix} = 0 \quad , \tag{3-22}$$

where the numerical an measurement noise is present in R_{12} and R_{22} only.

From equation 3-22, $[R_{22}][b] = 0$, and applying an SVD to the first matrix leads to

$$[R_{22}] = [U_1][S_1][V_1^H] \quad , \tag{3-23}$$

whose TLS solution is the last column of $[V_1]$ as in

$$[b] = [V_1]_{Q+1} \quad . \tag{3-24}$$

Now, having the vector $[b]$, and using equation 3-25, the coefficients vector $[a]$ can be determined.

$$[R_{11}][a] = -[R_{12}][b] \longrightarrow [a] = -[R_{11}]^{-1}[R_{12}][b] \quad . \tag{3-25}$$

As mentioned before, these a and b coefficients for the numerator and denominator polynomials can be transformed into poles and residues using equation 3-17. The general steps for Cauchy method is in Figure **3-7**.

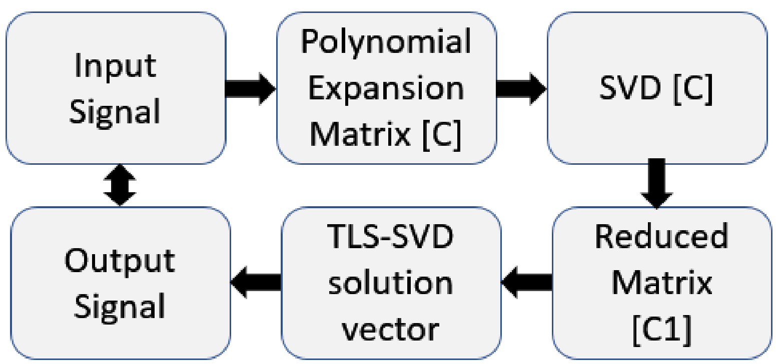

Figure **3-7**.: General step by step in Cauchy's method for CNR calculation in frequency domain signals.

A quick validation of the method is performed with the frequency-domain Transfer Function signal $Y(\omega) = \frac{0.5}{\omega+1} + \frac{5}{\omega+5} + \frac{7}{\omega+6} + \frac{9}{\omega+8}$, where the CNRs are located at $\omega = 1$, 5, 6 and 8. The reconstruction should be accurate and the poles in the complex plane well-placed.

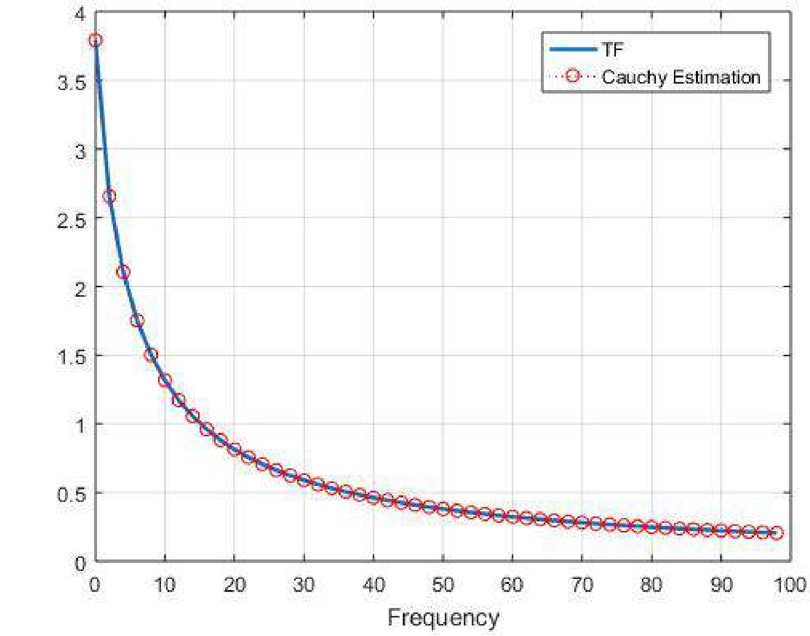

Figure **3-8**.: Frequency domain signal reconstruction using Cauchy's method

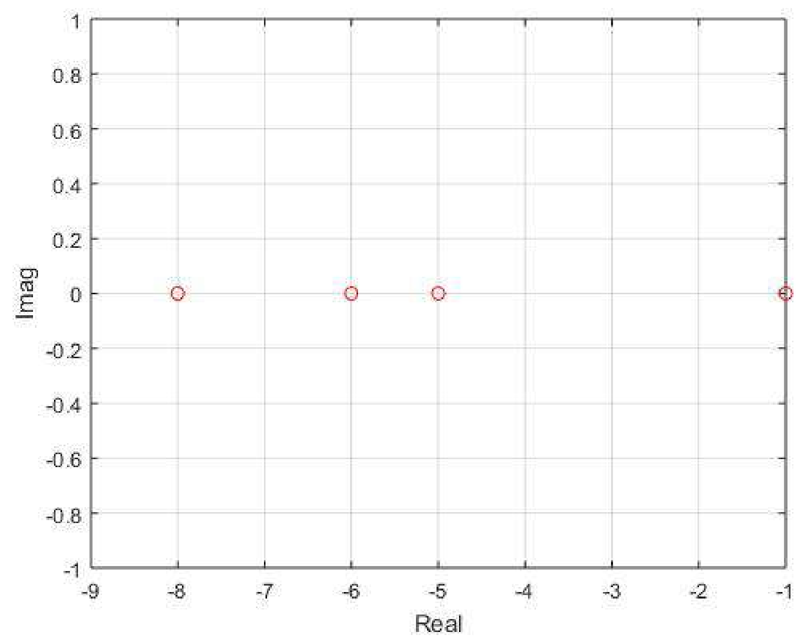

Figure **3-9**.: Poles calculated through Cauchy's method for a dummy input signal.

Figures **3-8** and **3-9** show the signal reconstruction and the resonances calculated. Again, the method works for a benchmark signal as the poles are situated correct.

3.6. Backscattering examples

A comparison between Prony, Cauchy and Matrix Pencil Methods for the extraction of CNRs provided an insight into the feasibility for a hardware-based algorithm implementation that could work in a real time implementation for GPR operations. Here, the analysis is performed using signals from three backscattering scenarios: simulation, free space and a sandbox. In chapter 4, the number of samples, the quality of the reconstructed signal and the execution time for a set of signals is compared and analyzed.

Figure **3-10** displays an example for the thin wire simulated response, the reconstruction and the poles calculated for each of the three methods.

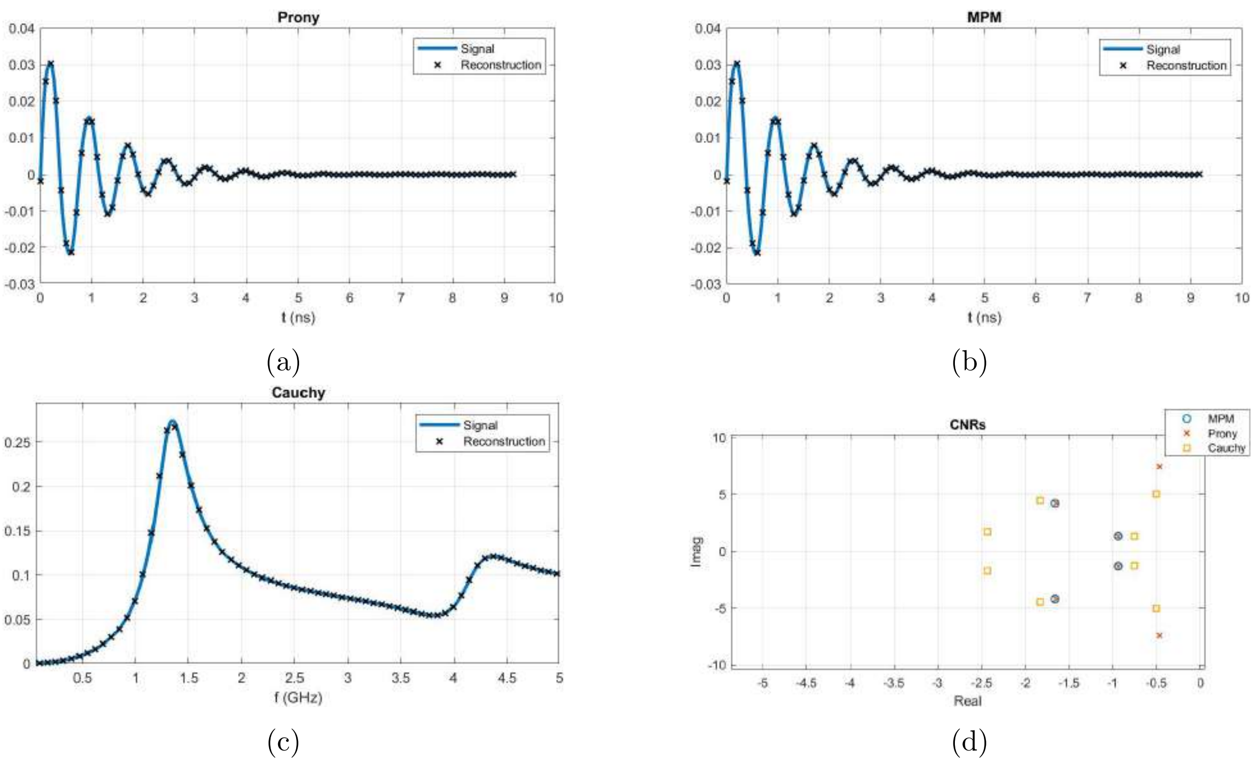

Figure **3-10**.: Thinwire (a) time domain response and Prony's based reconstruction, (b) time domain response and MPM based reconstruction, (c) frequency domain response and Cauchy based reconstruction and (d) calculated CNRs with MPM, Prony and Cauchy.

Now, before the CNRs can be calculated from a time-domain signal, only the Late Time Response should be taken into account. This is done to avoid direct wave reflections and consider only the natural resonance of the object. For frequency-domain signals, the complete spectrum is processed, however, a manual post-processing is applied.

In this scenarios, the complete set of CNRs from Cauchy is displayed and no manual post-processing is done, as the intention is to have an automatic system. For this reason, some of the resonances from Cauchy in Fig. **3-10**d have different real values than Prony or MPM.

An example of the backscattering scenarios for free-space and the corresponding reconstruction is shown in Figure **3-12**, and the basic experimental setup is shown in Figure **3-11**.

Figure **3-11**.: Basic setup for a metal cylinder backscattering scenario in free space.

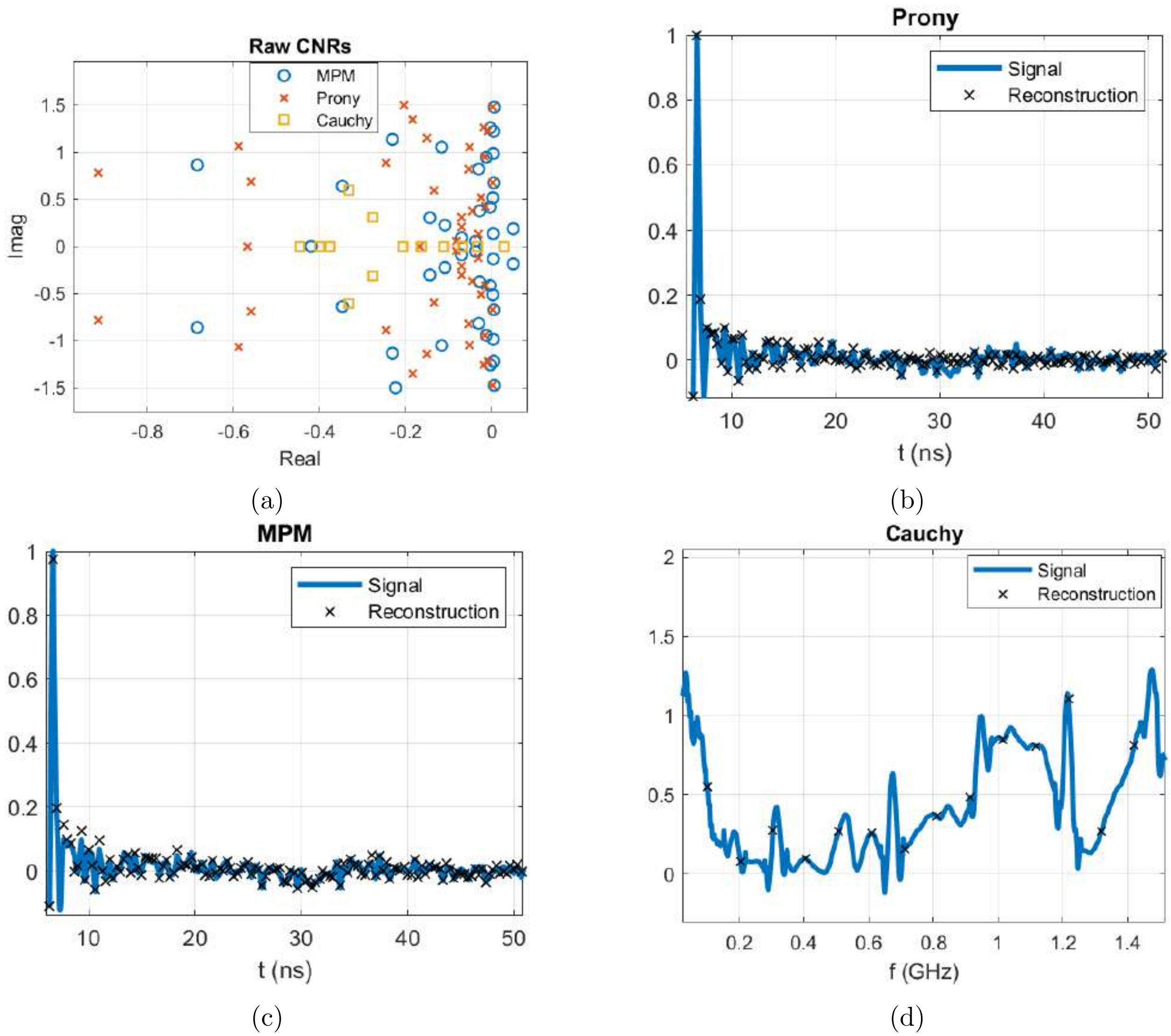

Figure **3-12**.: Metal cylinder Raw CNRs (a), (b) time domain frequency response and SVD-Prony's based reconstruction, (c) MPM based reconstruction and (d) frequency response and TLS-Cauchy based reconstruction.

First, the raw CNRs in Fig. **3-12**a shows all the resonances, including noise. Although these resonances lead to a reconstruction with an R^2 measure above 0.98 for both frequency and time domains (a good result), an automatic filter was designed to help the identification of the principal components of the objects, removing all resonances: 1) that are not complex conjugated; 2) with frequencies or imaginary parts greater than the maximum frequency; an 3) with positive real part. Also, only the poles in the positive imaginary axis will be shown.

After this process, and in order to identify the dominant poles, a 3 dimensional plot including not only the poles but the residues as well, as in Figure **3-13** shows the dominant resonances, which are the ones with the greater residue for each method. Here, MPM and Cauchy dominant poles can be identified easily, and Prony's should be analyzed closely.

After the automatic filter is applied, the output is displayed in Figure **3-14**, where the frequencies are at 0.601, 0.689 and 0.638 for Cauchy, Prony and MPM, indicating that the basic object dimensions are 237 mm, 207 mm and 223 mm approximately. The MPM is the most consistent with the metal cylinder height, 220 mm, and also is the best reconstruction with an $R^2 = 0.998$.

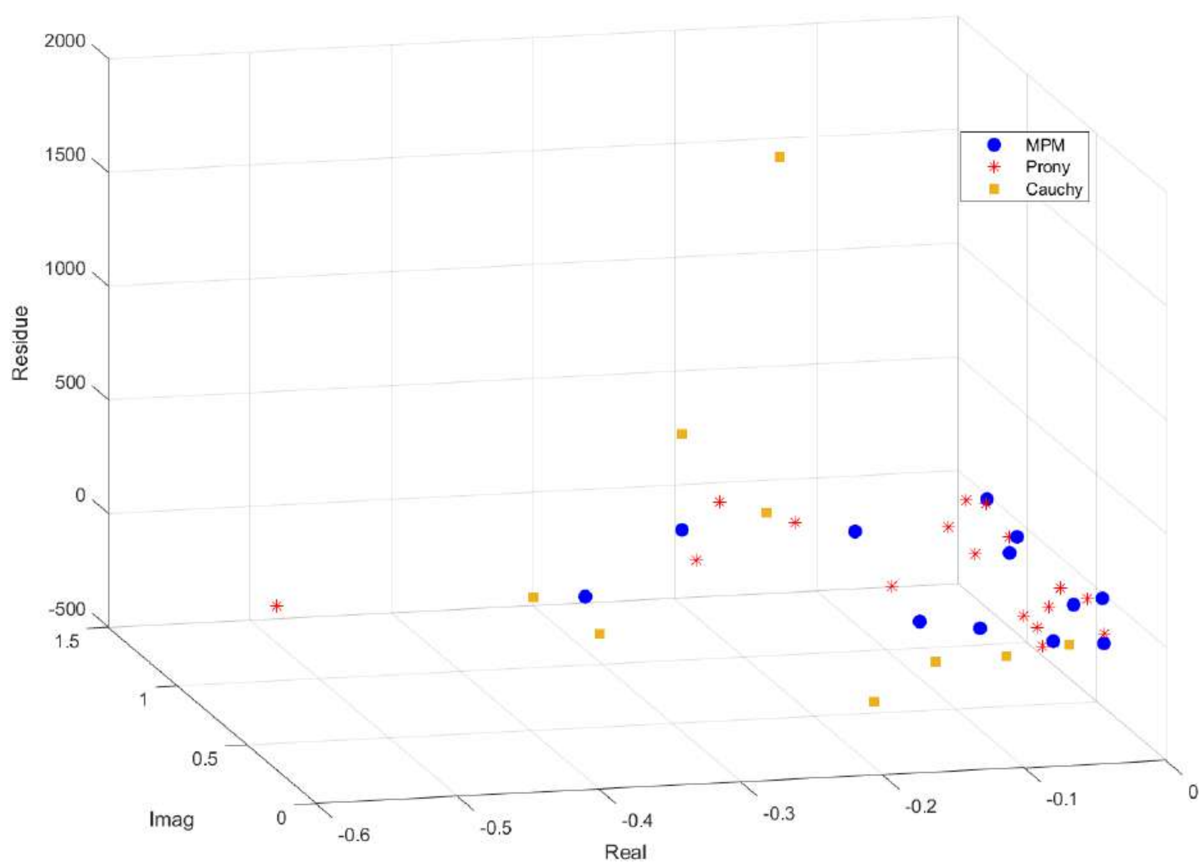

Figure **3-13**.: CNRs and the associated amplitude Residue

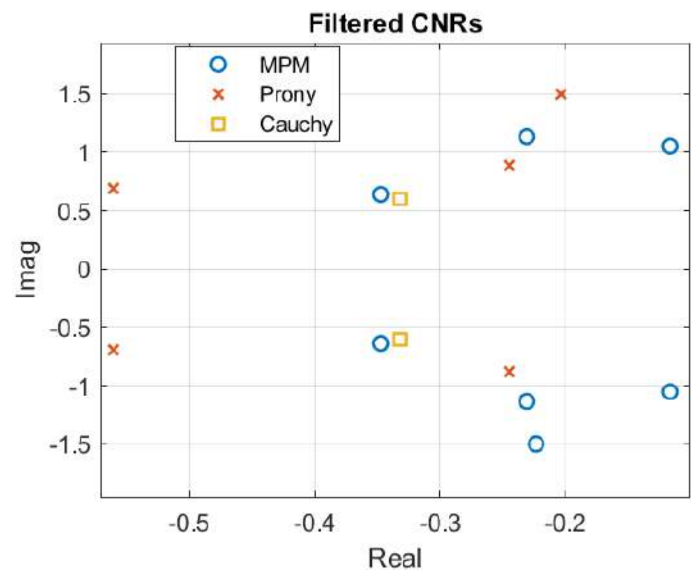

Figure **3-14**.: Filtered dominant poles for the metal cylinder in free space.

For the case of a metal can buried in sand, Figure **3-15** shows the filtered poles and the corresponding reconstructions. Here, the CNRs should be analyzed in detail as the principal components indicate a metal object with a size from $104mm$ to $119mm$, while the metal can is $115mm$. The MPM method is the most accurate in this manner, and provides also the best reconstruction of the signal. Again, the relationship between the residues and the associated real parts of the poles reconstruct the signal, but do not match exactly for all methods. This is because the amplitude (residue) and the frequency amplitude rely on each other and the soil electromagnetic parameters have not been taken into account yet. Furthermore, the most important feature is the resonant frequency, i.e., the complex part of the poles, and a small mismatch is acceptable in this case, and when the object is buried, a frequency shifting is expected depending on the soil electrical permittivity, which is treated in [42].

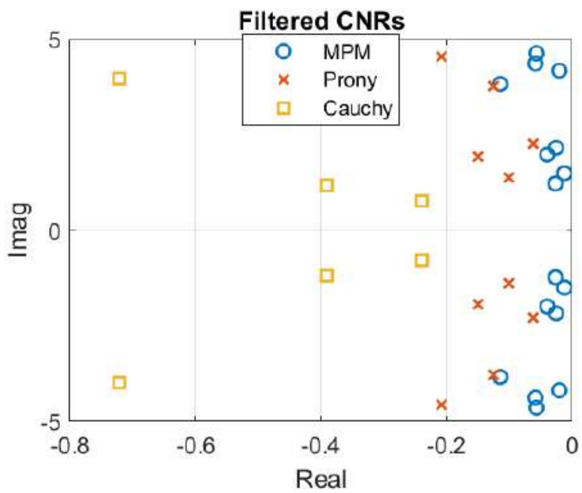

(a)

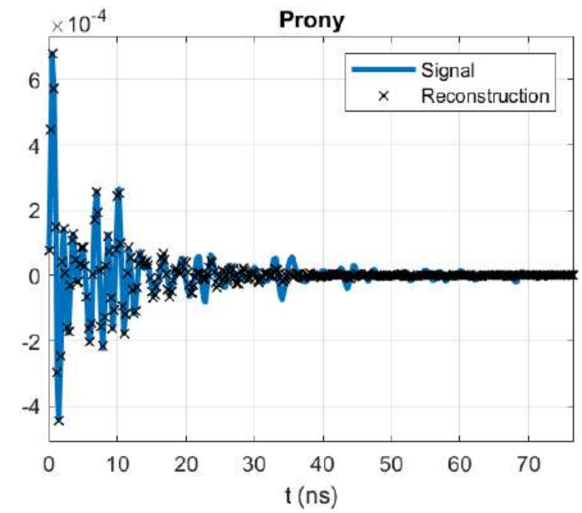

(b)

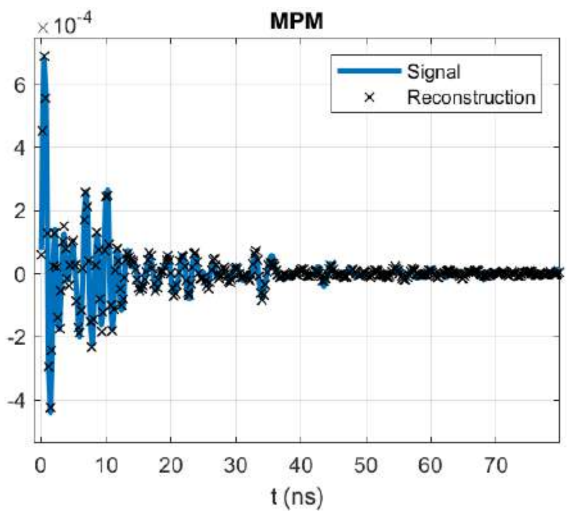

(c)

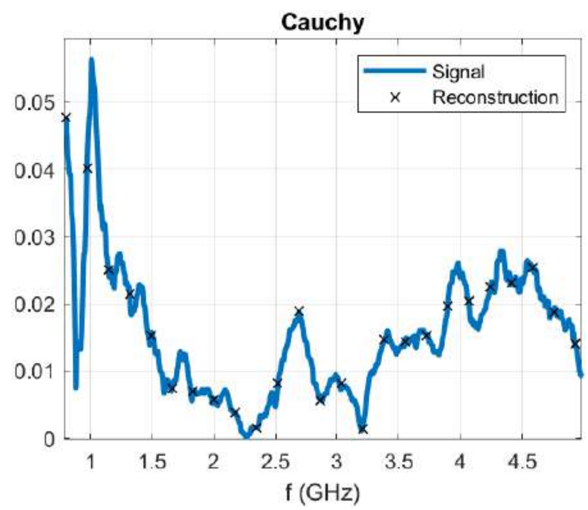

(d)

Figure **3-15**.: Metal can buried in sand (a) Filtered CNRs, (b) time domain frequency response and SVD-Prony's based reconstruction, (c) MPM based reconstruction and (d) frequency response and TLS-Cauchy based reconstruction.

3.7. Conclusions

This review of the Singularity Expansion Method focusing on the determination of the Complex Natural Resonances of metallic targets in simulation and experimental setups has been presented. First, a detailed explanation of the Prony, Matrix Pencil and Cauchy methods in time and frequency domain with constructed signals was given, also with examples of the CNRs calculated from the backscattered signals in simulation, free space and sandbox scenarios.

The first insight on these methods, before we move to the next chapter dedicated to the performance comparison, is that besides removing the clutter and noise from the input signals, either in time or frequency domain, the extracted poles also need a post-processing to filter numerical errors that lead to mistakes in the identification of the principal frequencies of the object. Although this is usually a manual task, the automation presented here is able to separate spurious poles from the resonances of interest without raising computer processing time significantly.

The validation of the CNR-based reconstruction of the signal through R^2 coefficient is necessary as a first validation of the CNRs extraction. This provided the first insight of the behavior of each algorithm and the means for the comparison with each other. There is a relationship between the R^2 and the object's principal frequency, i.e. if the reconstrucion is excellent, the CNRs calculated are stable and contain the principal frequency of the object. Here, Matrix Pencil Method results for both outperformed Cauchy and Prony's methods.

4. Computational efficiency and accuracy

In chapter 3, the Complex Natural Resonances Extraction Methods (CNREM) Prony, MPM and Cauchy were explained using also signals from simulated and experimental backscattering scenarios. These signals were part of a set composed of simulations in CST Microwave Studio, experiments in free space and buried objects in a sandbox. Here, the computational efficiency and accuracy of these methods was evaluated and compared with signal reconstruction accuracy, number of samples used and computing time. An study on the computational cost in terms of computational complexity in computer science can be done, however, as these methods rely on several SVDs, QR decompositions and TLS, the complexity is a factor of $O(mn^2)$, with input data matrix $m \times n$. The input size (or number of samples) is analyzed for this purpose [25].
The analysis of the advantages and disadvantages of each method is made to extract useful information from GPR signals, and also characterize them in computational cost and accuracy for the post-processing portable device-oriented automation.
For the simulated signals, the canonical objects in Table **4-1** were simulated in CST Microwave Studio, obtaining the time and frequency domain backscattering data in vacuum, with a plane wave in the frequency range from from 0 to 5 GHz. Three different angles for the measuring probe allowed us to have 12 simulation results.

	Dimensions (mm)
Thinwire	$l = 100$, $d = 2$
Sphere	$r = 50$
Plate	$l_1 = 100, l_2 = 100, h = 1$
Cylinder	$d = 50, l = 100, t = 1$

Table **4-1**.: Canonical objects simulated in three different positions

The experiments in free space used two Vivaldi antennas from RFSpace (TSA600) and a VNA up to 3 GHz as in Fig. **4-1**. In this case, the height was modified to obtain three different incident wave angles. For the sandbox experiments, a dual-polarized Vivaldi antenna separated 0.25 m from the surface of the sandbox measured a regular soda metal can and a metal plate, both buried 0.15 m below that surface. Figure **4-2** shows the general setup.

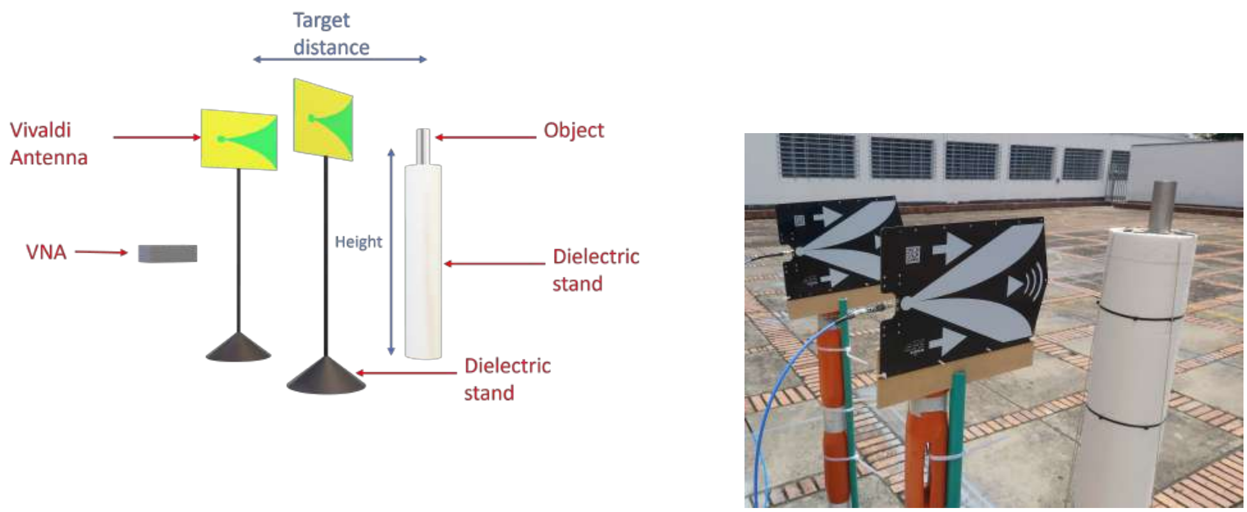

Figure **4-1**.: Basic experimental setup for free space backscattering scenarios.

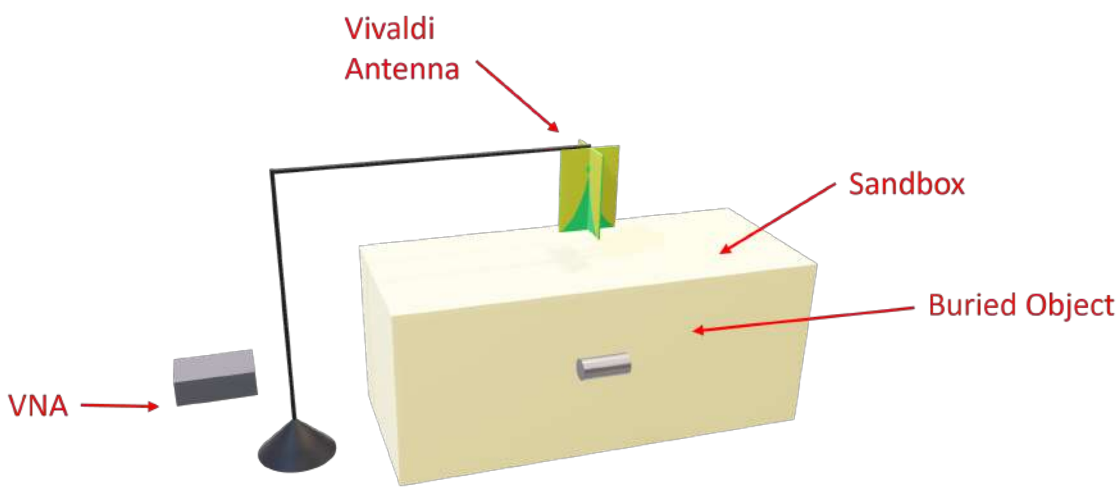

Figure **4-2**.: Sandbox experiments basic setup.

4.1. Accuracy

This validation and evaluation of how well the algorithms reconstruct the input signal so the poles can be validated in the initial stage of CNR-based object identification, is usually performed by an expert looking at the two data sets (original and reconstructed) in the same plot. For a numerical evaluation of the similarity between these two signals, the approach here is the R^2 measurement with values between 0 and 1 for no similarity or a perfect reconstruction respectively.

In total, 21 backscattering scenarios were evaluated for MPM, Prony and Cauchy reconstructed signals. The results for the accuracy comparison are in Table **4-2**, where averages for the simulation and experimental scenarios are shown, also with the total average.

If the averages are analyzed for every CNREM, as in Figure **4-3**, MPM has the higher results, i.e., the finest reconstruction of the signal in all scenarios. The difference comes mainly from the results for experimental signals, indicating that Prony and Cauchy methods are more sensitive to signal or numerical noise. Also, this difference becomes greater for buried objects, where the reflections of the inner and outer layer of the sand, or the clutter in general, imply a demanding signal processing task.

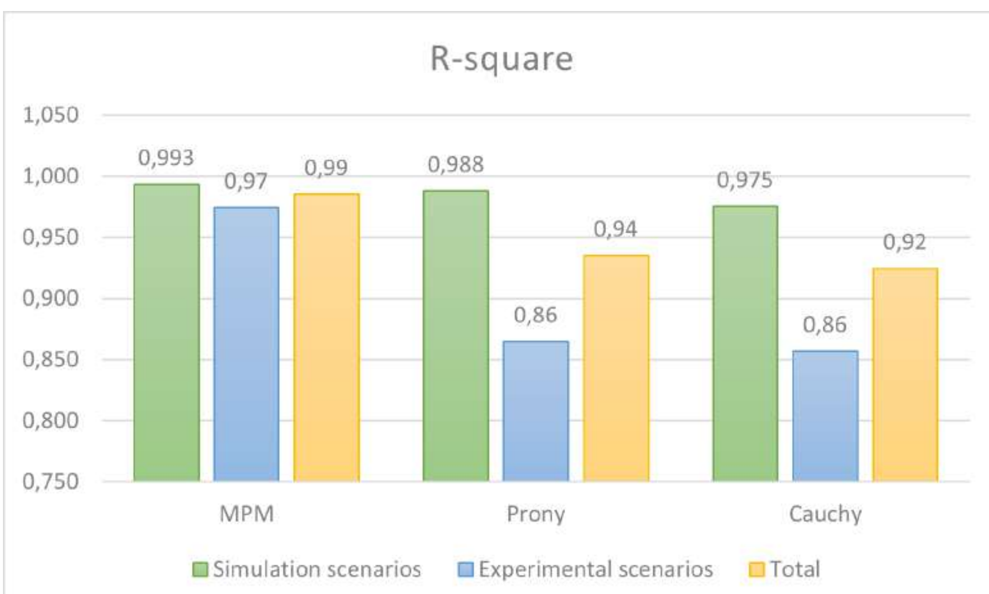

Figure **4-3**.: Comparison for CNREM accuracy in different backscattering scenarios.

		R^2		
		MPM	**SVD-Prony**	**TLS-Cauchy**
Simulation scenarios	**Thinwire**	1,000	1,000	0,887
		1,000	1,000	0,994
		1,000	1,000	0,996
	Cylinder	0,986	0,999	0,977
		0,998	0,999	0,949
		0,999	0,999	0,993
	Plate	0,999	0,999	1,000
		1,000	0,998	1,000
		0,998	0,998	1,000
	Sphere	0,991	0,964	0,990
		0,995	0,947	0,964
		0,953	0,952	0,951
	Average	0,993	0,988	0,975
Free space	**Metal cylinder**	0,995	0,995	0,831
		0,98	0,99	0,677
		0,998	0,995	0,883
Buried objects	**Metal can**	0,975	0,819	0,875
		0,972	0,792	0,913
		0,969	0,703	0,909
	Metal plate	0,967	0,748	0,869
		0,950	0,900	0,874
		0,961	0,840	0,880
	Average	0,97	0,86	0,86
	Total average	0,99	0,94	0,92

Table **4-2**.: R^2 coefficient for CNREM with simulation and experimentation signals

4.2. Number of samples

For the same backscattering scenarios, the number of samples used for every method that provided the best reconstruction was recorded, and the comparison is in Table **4-3**. The first fact is the substantial difference in samples for time and frequency domain methods by an approximate factor of 20 in the total average. Also, time-domain methods worked with the same number of samples in order to avoid any type of filter or signal decomposition.

		# of samples		
		MPM	**SVD-Prony**	**TLS-Cauchy**
Simulation scenarios	**Thinwire**	279	279	45
		281	281	45
		276	276	45
	Cylinder	818	818	40
		815	815	35
		805	805	35
	Plate	228	228	40
		229	229	40
		224	224	40
	Sphere	238	238	48
		238	238	48
		235	235	40
	Average	389	389	42
Free space	**Metal cylinder**	507	507	21
		507	507	23
		507	507	35
Buried objects	**Metal can**	2048	2048	50
		2048	2048	50
		2048	2048	60
	Metal plate	2048	2048	60
		2048	2048	60
		2048	2048	60
	Average	1534,33	1534,33	46,56
	Total average	879,76	879,76	43,81

Table **4-3**.: Number of samples for CNREM with simulation and experimentation signals

Summarizing as in Figure **4-4**, notice how there is a significant samples increase in Prony and MPM experimental scenarios as well. Again, this increase is more clear for buried objects experiments. Additionally, Cauchy sample set is more stable, and does not change considerably through all the data set.

4.3. Execution time

For processing this dataset, Matlab was runned in a computer with an intel core i7 and 32GB of RAM. A single algorithm loaded the signals offline and only the execution time of each CNREM was measured in the tenths of milliseconds. This is also an important step with the aim of an FPGA hardware acceleration design for real-time GPR landmine-detection

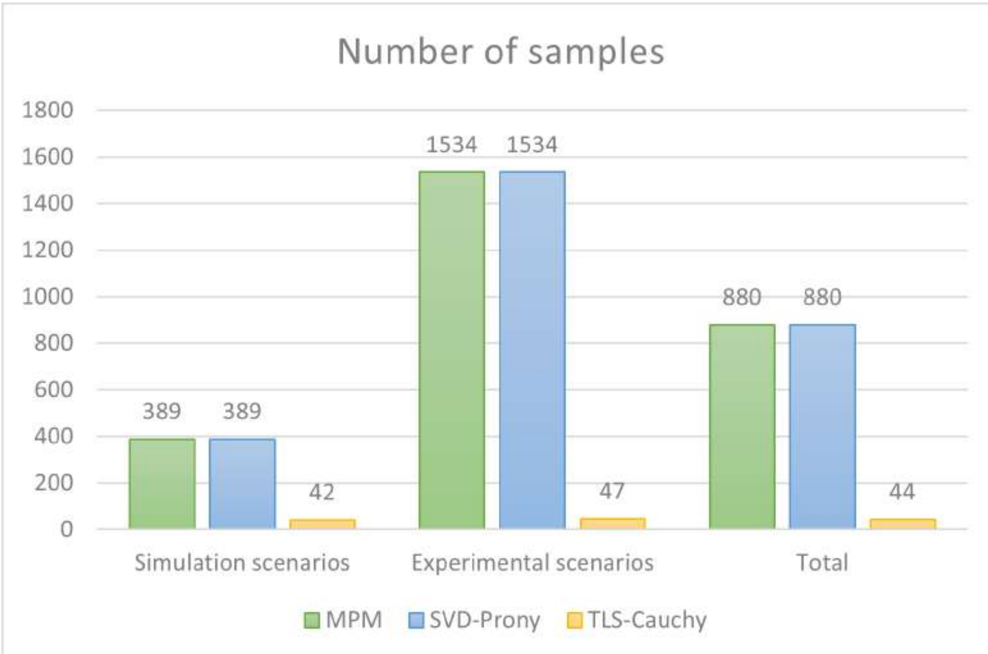

Figure **4-4**.: Frequency and time domain CNREM number of samples used for backscattering scenarios.

operations. The results are in Table **4-4**, where again, as in the reduced number of samples, Cauchy outperforms time-domain methods with a faster performance.

		Execution time (ms)		
		MPM	**SVD-Prony**	**TLS-Cauchy**
Simulation scenarios	**Thinwire**	6,1	14,3	35,5
		7,7	20,1	42,7
		8,5	16,9	38,5
	Cylinder	37,0	43,2	39,2
		40,0	41,7	40,8
		35,4	34,3	34,9
	Plate	6,0	13,8	37,5
		6,5	16,3	32,3
		6,0	15,2	37,4
	Sphere	7,0	14,8	33,8
		6,8	16,8	37,2
		7,0	15,7	36,3
	Average	14,5	21,9	37,2
Free space	**Metal cylinder**	39,4	48,7	43,4
		46,6	51,4	47,7
		42,5	47,5	41,7
Buried objects	**Metal can**	977,0	318,0	35,0
		1015,0	404,0	36,4
		954,0	255,0	35,2
	Metal plate	943,0	331,0	35,1
		1015,0	416,0	36,0
		945,0	406,0	37,1
	Average	664,17	253,07	38,62
	Total average	292,93	120,99	37.8

Table **4-4**.: Execution time for CNREM with simulation and experimentation signals

The average information in Figure **4-5** Cauchy's stability for every radar scenario, clearly the fastest of all three methods. For MPM and Prony, the execution time increases in experimental scenarios, mostly for buried objects.

Simulation signals do not show this difference, and would show these methods as very similar in execution time. However, it is clear that, as Cauchy operates with less samples, and despite having a different numerical approach, it operates a lot faster than time-domain based methods for extracting CNRs.

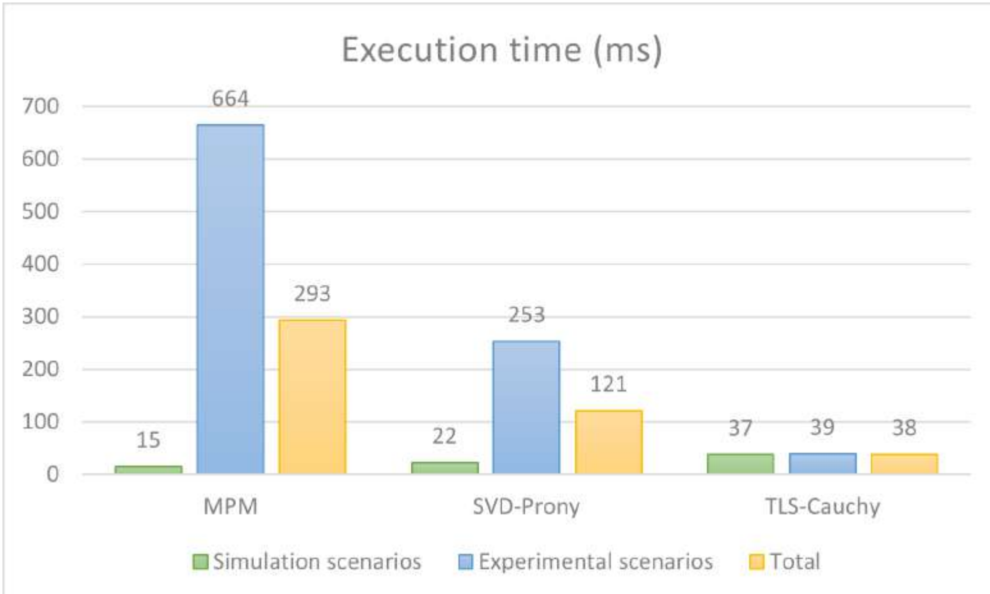

Figure **4-5**.: Execution time per CNREM on an Intel Core i7 with a 32 GB RAM. It is noticeable to see that in all cases the lowest execution time is obtained with TLS-Cauchy.

4.4. Hardware implementation suitability

For a hardware-based CNR extraction algorithm that works in real-time GPR operations, the previous insight on the number of samples, execution 'time and accuracy could be considered together. ψ_{R^2} is the hardware implementation suitability factor, A_{R^2} the accuracy from R^2, t_e is the execution time in seconds and N the number of samples. Considering this suitability factor increases with accuracy and decreases with time and the number of samples used, then ψ_{R^2} is directly proportional to A and inversely proportional to N and t_e, or $\psi_{R^2} \propto A_{R^2}\frac{1}{N}\frac{1}{t_e}$. A simple approach for this is in Eq. 4-1.

$$\psi_{R^2} = \frac{A_{R^2}}{Nt_e} \tag{4-1}$$

Since the computational complexity has not changed, the linear relation between the number of samples and time executed in this hardware implementation suitability factor performs a comparison for the CNR extraction algorithms. Also, as R^2 accuracy has values from 0 to 1, then is a scale factor for this performance ratio as well. Table **4-5** presents the calculated values where Cauchy method has the best result. This is due to its completion time combined with the advantage of using fewer samples being more important that the accuracy in this manner.

Although in time-domain MPM has a better reconstruction, these results highlights Prony

	MPM	Prony	Cauchy
Simulation	176,2	115,9	628,3
Free space	45,6	39,8	683,7
Buried	0,5	1,1	437,1
Total	**3,8**	**8,8**	**558,3**

Table **4-5**.: Hardware implementation suitability factor for backscattering scenarios and in total. the values here were multiplied by 1×10^3 for a better comparison.

as more suitable for a hardware implementation, because despite its low noise tolerance, its processing is faster.

4.5. Conclusions

A factor for evaluating hardware implementation suitability has been presented, leading to a simple but yet effective relation between t_e, N and A_{R^2} for the comparison of CNREM in pursuance of a hardware implementation. This hardware suitability factor, i.e. the execution time, accuracy and number of samples used, indicates that Cauchy is the more suitable method for a hardware implementation. Be that as it may, its reconstruction accuracy could be improved, mainly for radar scenarios.

The CNR calculation for simulated signals have similar execution times for all the methods evaluated. However, the number of samples in radar scenarios significantly increases in time-domain methods, leading to increasing processing time also. When the radar scenario is GPR, the value of this gap increases even more leaving Cauchy method as the best performer.

Here, MPM has the best reconstruction accuracy for all scenarios. If the fidelity is crucial, then this method should be used instead. In time domain, MPM is more accurate for noisy environments, but the overall result is that Prony is more suitable for a time-domain HW implementation because its execution time is less. On the other hand, in frequency domain, Cauchy has less samples and its execution is faster, and has the best results because the reconstruction accuracy difference with the other methods is not substantial.
Depending on the application, each method has its own advantages and disadvantages. For example, if a high reconstruction accuracy is desired, then MPM is to be used. If execution time is critical, then Prony is the best option in time-domain, and Cauchy in frequency domain. Also, if only a few samples are available, Cauchy is the best option. Again, decreasing MPM time or increasing Prony's and Cauchy's accuracy could be the course of action for improving CNREM performance.

5. Vector Fitting-Cauchy Method (VCM)

In Chapter 4, one of the conclusions positioned Cauchy's method as the more suitable for a hardware implementation, although its reconstruction accuracy for the calculated CNRs validation was not the best between the methods evaluated. A novel rational function approximation based in both Cauchy and Vector Fitting is proposed and evaluated here in order to increase this accuracy in the frequency domain. This has been previously presented in [55] and [?]. The comparison between the reconstructed and the input data, instead of R^2 as in the previous chapter, is now carried on by the Feature Selective Validation comparison which, proposed by Duffy et.al., evaluates the similarity of two electromagnetic responses as it would be executed by an expert engineer [56]. After a review of the Vector Fitting method in Section 5.1, the VCM is presented in Section 5.2. Then, the validation and comparison with Cauchy's method is shown in Section 5.3.

5.1. Vector Fitting method

This method was presented in 1999 by Gustavsen and Semlyen [57], and corresponds also to a rational function approximation as in Eq. 5-1.

$$f(s) = \sum_{n=1}^{N} \frac{c_n}{s - a_n} + d + sh \quad . \tag{5-1}$$

With a set of initial poles defined or proposed, a problem to be linearly solved can be constructed as in Eq. 5-2. The idea is to multiply the function $f(s)$ by an unknown function $\sigma(s)$ that contains the same poles $\bar{a_n}$. N is the assumption for the number of poles or complex resonances set, while h and d are real.

$$\begin{bmatrix} \sigma(s) f(s) \\ \sigma(s) \end{bmatrix} = \begin{bmatrix} \displaystyle\sum_{n=1}^{N} \frac{c_n}{s - \bar{a}_n} + d + sh \\ \displaystyle\sum_{n=1}^{N} \frac{\tilde{c}_n}{s - \bar{a}_n} + 1 \end{bmatrix} \tag{5-2}$$

With $\bar{a_n}$ as the initial resonances, this augmented problem can be represented as in Eq. 5-3 if the second row is multiplied by $f(s)$. This can also be represented as in Eq. 5-4.

$$\sum_{n=1}^{N} \frac{c_n}{s-\bar{a}_n} + d + sh = \left(\sum_{n=1}^{N} \frac{\tilde{c}_n}{s-\bar{a}_n} + 1 \right) f(s) \tag{5-3}$$

$$(\sigma f)_{fit}(s) = \sigma_{fit}(s) f(s) \tag{5-4}$$

The functions $(\sigma f)_{fit}(s)$ and $\sigma_{fit}(s)f(s)$ can be organized as

$$(\sigma f)_{fit}(s) = h\frac{\prod_{n=1}^{N+1}(s-z_n)}{\prod_{n=1}^{N}(s-\bar{a}_n)} \quad \text{and} \quad \sigma_{fit}(s) = \frac{\prod_{n=1}^{N}(s-\tilde{z}_n)}{\prod_{n=1}^{N}(s-\bar{a}_n)} \quad , \tag{5-5}$$

and if these two functions are multiplied to find $f(s)$ as in Eq. 5-6, then the poles of $f(s)$ become equal to the zeros in $\sigma_{fit}(s)$.

$$f(s) = (\sigma f)_{fit}(s)\sigma_{fit}(s) = h\frac{\prod_{n=1}^{N+1}(s-z_n)}{\prod_{n=1}^{N}(s-\tilde{z}_n)} \quad . \tag{5-6}$$

Now the calculation is reduced to the solution of $\tilde{c}_n$ in Eq. 5-3 as an overdetermined linear problem in the form $Ax = b$. After the poles have been calculated, the residue calculation can be achieved replacing a_n with $\tilde{c}_n$ in Eq. 5-1, which is again solved with TLS.

Although the function approximation can be accurate, this method is not able to identify the initial set of resonances in the system or its location from scratch. In other words, there is no system order calculation, or a determination of the CNRs of a backscattered signal in frequency domain by itself. For this reason, this method can not be considered as a Complex Natural Resonance extraction method.

5.2. VCM

The Vector fitting-Cauchy Method (VCM) is based in the rational function approximation of Eq. 5-7 for the assumed LTI frequency function $Y(s)$, with numerator and denominator polynomial coefficients u_k and v_k, and an initial system order $P = (N-3)/2$ and $Q = P+1$.

$$Y(s) = \frac{\sum_{k=0}^{P} u_k s_i^k}{\sum_{k=0}^{Q} v_k s_i^k} = \frac{U(s)}{V(s)} \tag{5-7}$$

A straightforward solution for u_k and v_k can be obtained with $U(s) - Y(s)V(s) = 0$, where the coefficients vector can be separated as follows:

$$[U \quad -V]\begin{bmatrix} u \\ v \end{bmatrix} = 0 \quad \text{or} \quad [C]\begin{bmatrix} u \\ v \end{bmatrix} = 0 \quad , \tag{5-8}$$

where the matrix $[C]$ can be constructed as in Eq. 5-9 for the N number of complex frequency samples f_n.

$$[C] = \begin{bmatrix} 1 & f_1 & \cdots & f_1^P & -Y_{f_1} & -Y_{f_1}f_1 & \cdots & -Y_{f_1}f_1^Q \\ 1 & f_2 & \cdots & f_2^P & -Y_{f_2} & -Y_{f_2}f_2 & \cdots & -Y_{f_2}f_2^Q \\ \vdots & \vdots & \ddots & \vdots & \vdots & \vdots & \ddots & \vdots \\ 1 & f_N & \cdots & f_N^P & -Y_{f_N} & -Y_{f_N}f_N & \cdots & -Y_{f_N}f_N^Q \end{bmatrix} \tag{5-9}$$

The Singular Value Decomposition (SVD),

$$[U][S][V]'\begin{bmatrix} u \\ v \end{bmatrix} = 0 \quad , \tag{5-10}$$

is used to determine the rank of the matrix $[C]$. The number of diagonal elements of $[S]$, σ_M, greater than the threshold $\sigma_M/\sigma_{max} = 10^{-p}$ (with p as the number of significant digits), is the number of coefficients $P+Q+1$. From here, the new values for P and Q can be found keeping $Q = P + 1$.
Now, with the system order, the matrix $[C]$ is reconstructed as $[C1]$ leading to Eq. 5-11. Here another SVD is computed to find the TLS solution vector showed in Eq. 5-12 for u_k and v_k as the last column of the matrix $[V]$.

$$[C1]\begin{bmatrix} u \\ v \end{bmatrix} = 0 \quad \longrightarrow \quad [U1][S1][V1]'\begin{bmatrix} u \\ v \end{bmatrix} = 0 \tag{5-11}$$

$$\begin{bmatrix} u \\ v \end{bmatrix} = [V]_{P+Q+2} \quad . \tag{5-12}$$

These are the initial Complex Natural Resonances of the system, which are sensitive to noise in the signal and the numerical noise introduced by the number of samples (up to the power of Q in $[C]$ and $[C1]$). A correction and a manual filtering would still be needed for spurious poles. For this reason, the following rational function approximation is considered again in Eq. 5-13 with the numerator and denominator coefficients obtained from Eq. 5-12.

$$Y(s) = \frac{u_P s^P + u_{P-1}s^{P-1} + \cdots + u_0}{v_Q s^Q + v_{Q-1}s^{Q-1} + \cdots + v_0} = \frac{R_1}{s-a_1} + \frac{R_2}{s-a_2} + \cdots + \frac{R_N}{s-a_N} \quad . \tag{5-13}$$

This can be transformed into Eq. 5-14 using the Vector Fitting analysis with functions $(\sigma f)_{fit}(s)$ and $\sigma_{fit}(s)f(s)$ of Eqs. 5-3 and 5-4, where R_n and $\tilde{R}_n$ are the residues and poles to be calculated.

$$\sum_{n=1}^{N} \frac{R_n}{s - a_n} + d + sh - \sum_{n=1}^{N} \frac{\tilde{R}_n}{s - a_n} f(s) \approx f(s) \tag{5-14}$$

A Least Square approach in the form of $Ax = b$ is used for the solution of this problem. For this, the matrices are constructed for every frequency point i as follows:

$$A_i = \begin{bmatrix} \frac{1}{si - a_1} & \cdots & \frac{1}{si - a_N} & 1 & s_i & \frac{-f(s_i)}{s_i a_1} & \cdots & \frac{-f(s_i)}{s_i a_N} \end{bmatrix} \quad , \tag{5-15}$$

$$x = \begin{bmatrix} R_1 & \cdots & R_N & d & h & \tilde{R}_1 & \cdots & \tilde{R}_N \end{bmatrix}^T \quad \text{and} \tag{5-16}$$

$$b_i = f(s_i) \quad . \tag{5-17}$$

The vector x contains the residues $\tilde{R}_n$, which are also the poles a_n of $f(s)$. Using these poles in Eq. 5-13, i.e. solving the following equation for R_n with another Least Square approach, results in the calculation of the Residues and poles of the input $f(s)$.

$$f(s) = \sum_{n=1}^{N} \frac{R_n}{s - \tilde{R}_n} + d + sh \quad , \tag{5-18}$$

With both the complex residues R_n and the poles a_n, the approximation of the input frequency signal $f(s)$ is completed. An overview of the method is shown in Fig. **5-1**

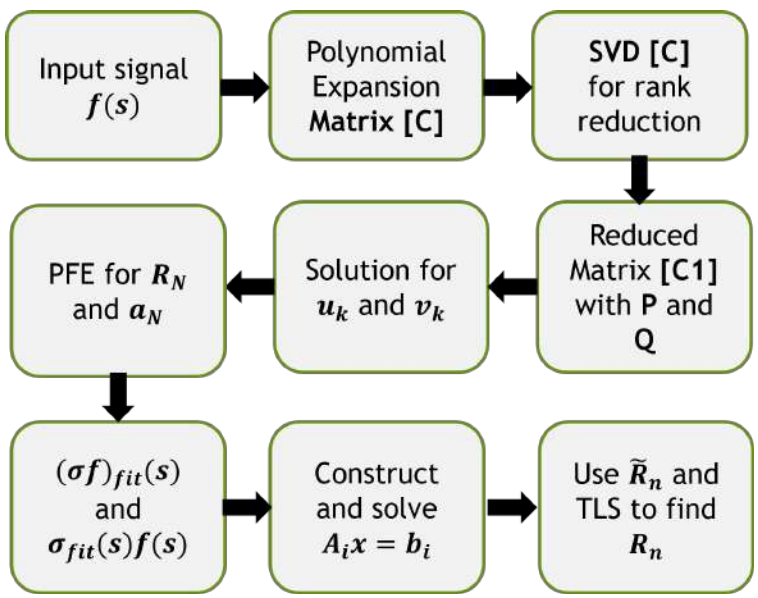

Figure **5-1**.: VCM algorithm calculating CNRs from a frequency domain input signal. A reconstructed signal could be compared to the input.

5.3. Validation and comparison

A set of simulated and experimental backscattering signals was constructed in order to validate VCM signal reconstruction and CNRs in contrast to Cauchy's. Here, as in Chapter 3, the complete collection of resonances is plotted in the complex plane, with no manual filtering, with the purpose of an automated system design. For this reason, the plots could have resonances considered as errors, because they have positive real part, are not conjugated or out of the frequency range. Also, both the real and imaginary part of the response were used for the calculation, although the plots show only magnitudes.

First, the simulation and experimental scenarios are explained with one example each. Then, the results for the whole set of simulations of VCM and the comparison with Cauchy will be shown.

5.3.1. Canonical objects simulation

A perfectly conducting thin wire, sphere, plate and cylinder were illuminated with a plane wave in CST Microwave Studio. The backscattered electric field measurements for different angles was analyzed with Complex Natural Resonances Extraction Methods (CNREM) in frequency domain.

An example of the backscattered signal is shown in Fig. **5-2**, where the metal sphere response is reconstructed with both frequency domain methods. Here, the difference between the two reconstructions is small compared to the dimension of the data, but will be quantified later. Fig. **5-3** displays the CNRs in the complex plane for the same scenario. Notice how the number of resonances remains the same for both methods, but their location is different. Some Cauchy calculated resonances exceed the frequency range in the imaginary part and are non-conjugated, while VCM has only one.

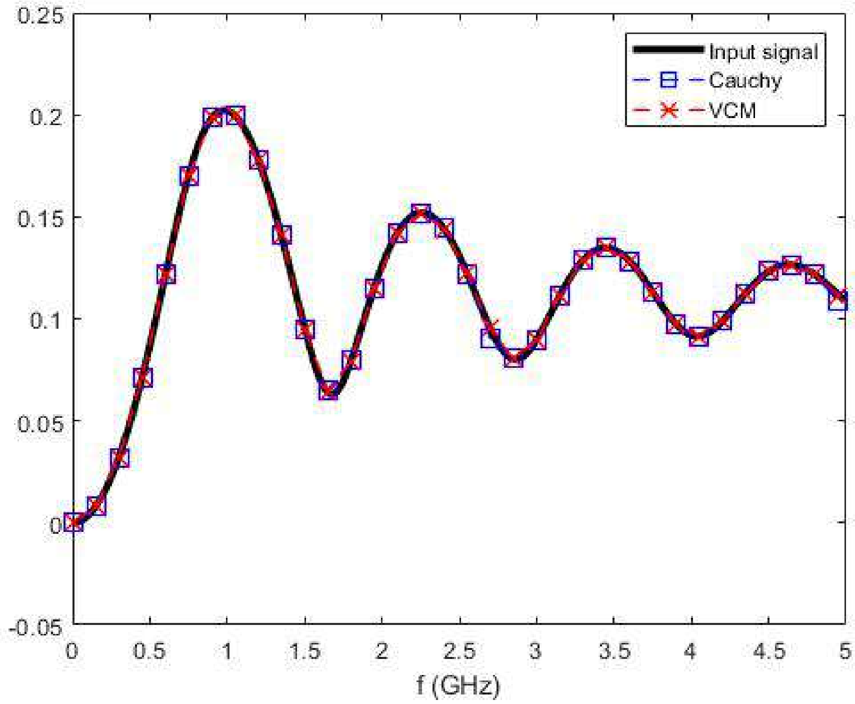

Figure **5-2**.: PEC sphere simulated response up to 5 GHz, VCM and Cauchy's signal reconstructions based in the CNR calculated.

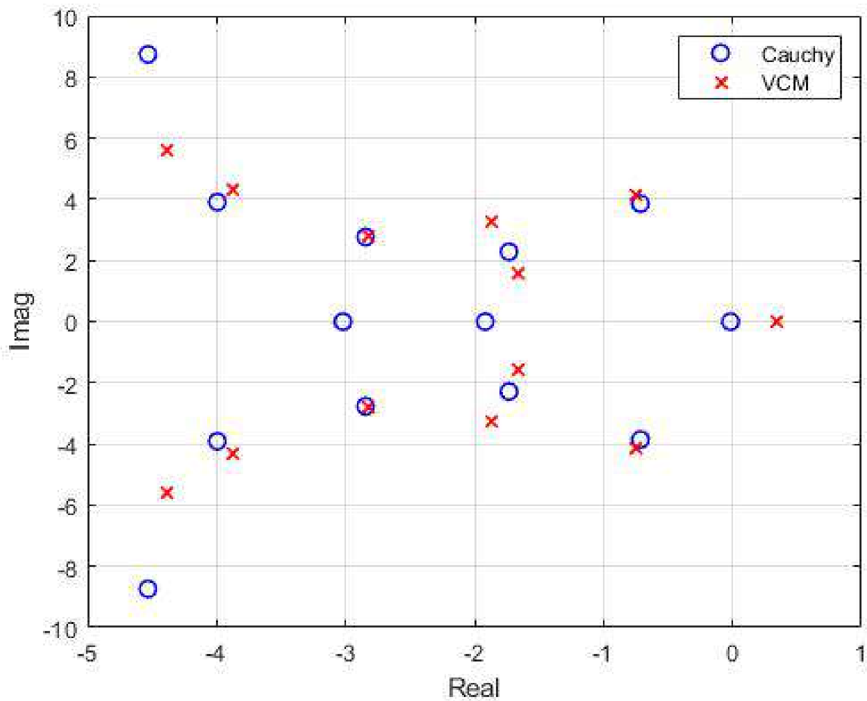

Figure **5-3**.: Complex plane locations of the CNRs calculated for the PEC sphere with Cauchy and VCM methods.

5.3.2. Experimental scenarios

A metal corner reflector, a metal cylinder, and an metal detonator commonly used in Improvised Explosive Devices (IEDs) in Colombia, were used as targets for the backscattering scenarios.

Free space

For the free space experiments, the setup is similar to that of Chapter 4, but his time in a different open field also displayed in Figs **5-4** and **5-5**.

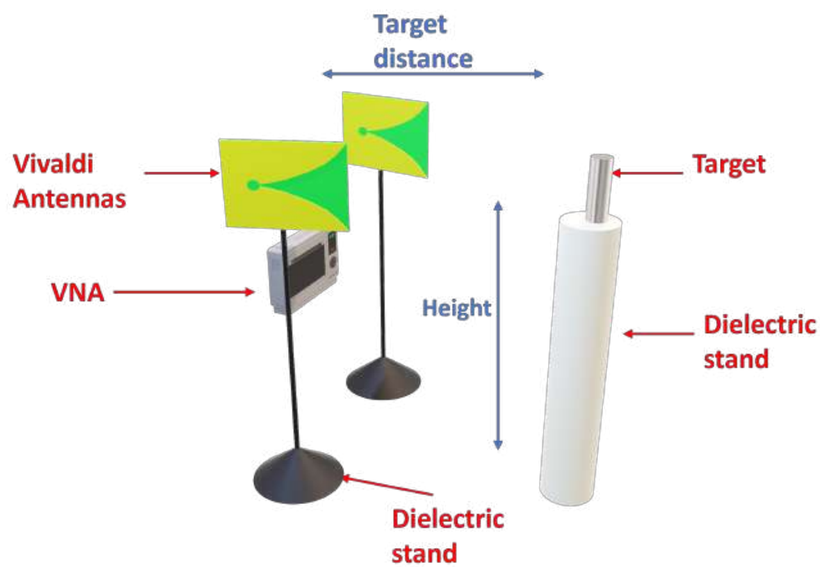

Figure **5-4**.: Free space experimental setup for frequency domain CNR calculations.

Figure **5-5**.: Metal cylinder for free space experimental setup in frequency domain CNR calculations.

Again, both the real and imaginary part of the response are used for the calculations, but the images show only the magnitude for a visual comparison.

As an example of the frequency domain response and the CNREM results, Fig. **5-6** shows the input signal of a metal cylinder alongside the corresponding reconstructions, and Fig. **5-7** shows the complex plane with the calculated resonances.

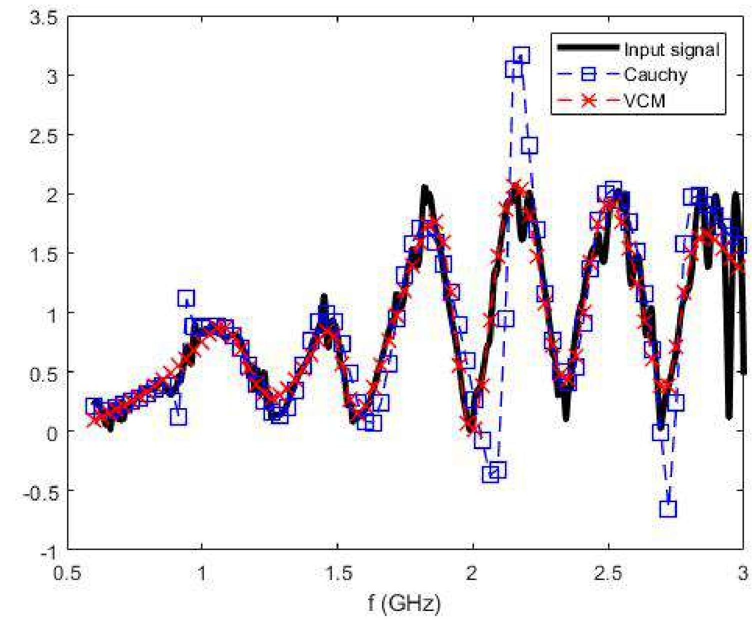

Figure **5-6**.: Frequency domain backscattered signal obtained from a metal cylinder in free space at 60 cm.

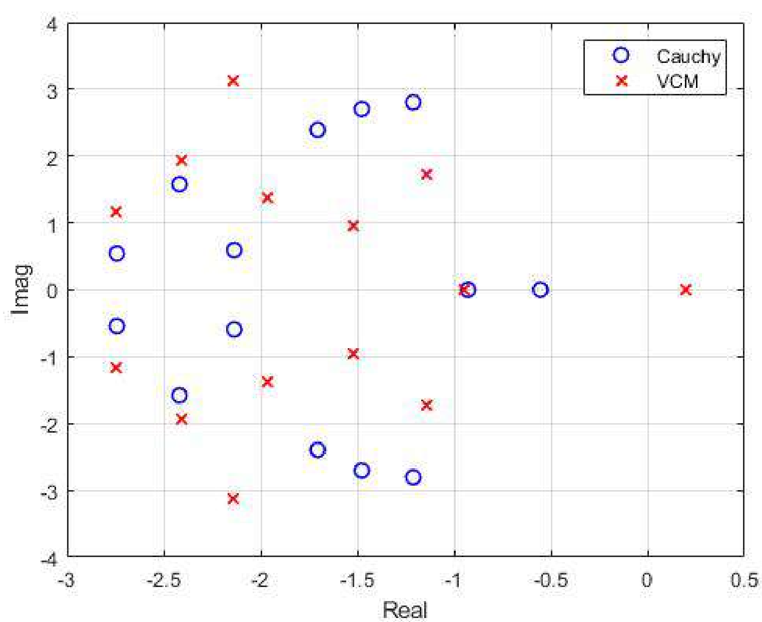

Figure **5-7**.: CNRs calculated with Cauchy and VCM used to reconstruct the backscattered signals of the metal cylinder in free space.

Among the multiple resonances identified by VCM, the one at 1.97 GHz represents an object dimension of 151.76 mm, while the height of the cylinder height for this experiment is 150 mm.

Buried targets

For the buried objects experiments, the setup is shown in Figs. **5-8** and **5-9**, where the antenna to target distance was 0.6 m, and the target was buried 0.15 as common IEDs manual deploying method.

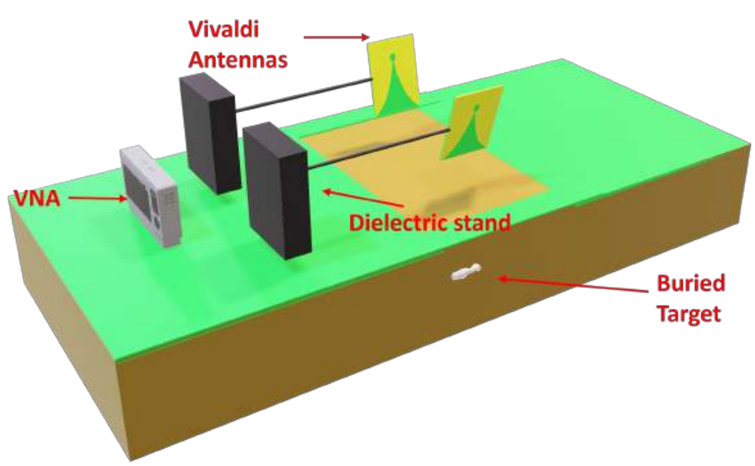

Figure **5-8**.: Buried targets experimental setup for frequency domain CNR calculations.

The vegetation and possible clutter was removed beforehand, including the evaluation and removal of background noise, antennas cross-talk and unwanted reflections as in the methodology presented in [4].

Figure **5-9**.: Buried metal IED detonator and Vivaldi antennas for GPR measurements.

This time, the example showed in Fig. **5-11** corresponds to the metal IED detonator in Fig. **5-10**, whose length is 55 mm and diameter is 4 mm.

Figure **5-10**.: Electric IED detonator commonly used in Colombia. The approximate dimension is 54 mm with a diameter of 4 mm.

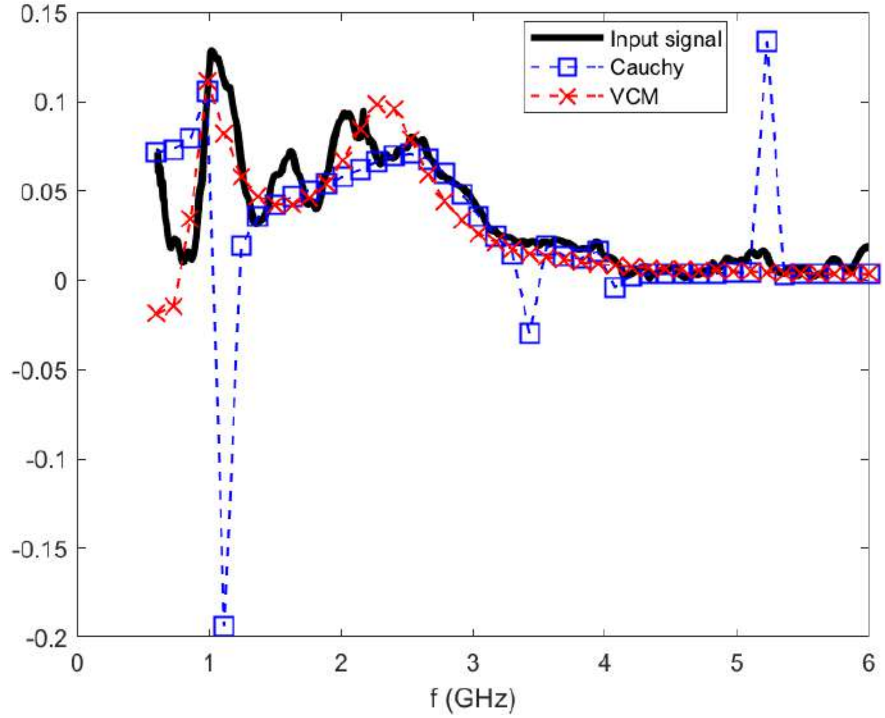

Figure **5-11**.: Backscattering signal reconstruction with Cauchy and VCM methods corresponding to an electric metal detonator for IEDs in Colombia.

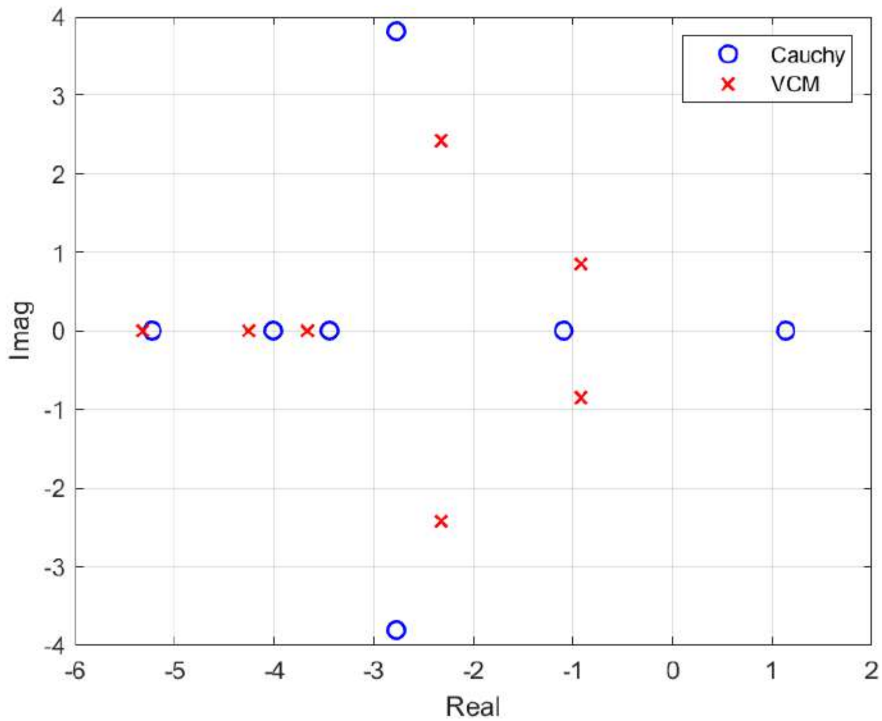

Figure **5-12**.: CNRs calculated with both Cauchy and VCM methods using the frequency response of an electric metal detonator for IEDs in Colombia.

The resonance identified by VCM at frequency 2.47 GHz is related to a target length of 57.7 mm, which is close to the 55 mm of the detonator length.

5.3.3. Results

For a total of 30 frequency response signals encompassing simulation, free space and underground objects, the reconstruction accuracy was evaluated using the Feature Selective Validation method. It provides a numerical value of the similarity between the input signal and the recreated one using the CNRs calculated, with the categories of Table **5-1**.

FSV categories for result value v	
Excellent	$v <= 0.1$
Very good	$0.1 < v <= 0.2$
Good	$0.2 < v <= 0.4$
Fair	$0.4 < v <= 0.8$
Poor	$0.8 < v <= 1.6$
Extremely poor	$v > 1.6$

Table **5-1**.: Similarity categories for two signals, according to FSV method results.

	FSV	# of samples	Execution time (ms)
Thinwire	0,001	37	98,5
	0,001	37	99,7
	0,002	37	118,9
Cylinder	0,063	21	95,3
	0,041	21	95,7
	0,014	21	92
Plate	0,0001	21	95,8
	0,0002	21	94,8
	0,0004	21	97,3
Sphere	0,02	37	102
	0,077	37	122,1
	0,037	37	105,6
Average	**0,021**	**29**	**101**

Table **5-2**.: Simulated scenarios FSV results for VCM, with execution time and number of samples used.

The average FSV result for the simulated signals is 0.021 and 0.1989 for the experimental scenarios, which fall into the *Excellent* and *Very Good* categories respectively. The complete results including the number of samples and execution time used in every scenario is presented in Tables **5-2** and **5-3**.

			FSV	# of samples	Execution time (ms)
Experimental scenarios	Free space	Corner reflector	0,18	37	96,07
			0,076	37	97,2
			0,121	37	97,2
		Metal cylinder	0,124	37	171,7
			0,119	37	99,1
			0,164	37	103,6
		Detonator	0,171	37	103,3
			0,155	37	98,8
			0,111	37	107,2
	Buried objects	Corner reflector	0,275	30	100,2
			0,262	30	98
			0,277	30	99,3
		Metal cylinder	0,381	30	99,8
			0,329	30	100,4
			0,204	30	104,2
		Detonator	0,322	30	101,1
			0,126	30	106,1
			0,183	30	98,4
	Average		0,198	33	104

Table **5-3**.: Free space and buried objects scenarios FSV results for VCM, with execution time and number of samples used.

FSV results for VCM and Cauchy are also compared, as in Fig. **5-13**. The average result is 0.161 for Cauchy and 0.128 for VCM, however, if only the experimental scenarios are analyzed, then VCM shows an improvement of more than 24% for the values of 0.262 for Cauchy and 0.128 for VCM. This means that VCM is able to calculate the CNR of an object and has an improved reconstruction for this simulations and experiments.

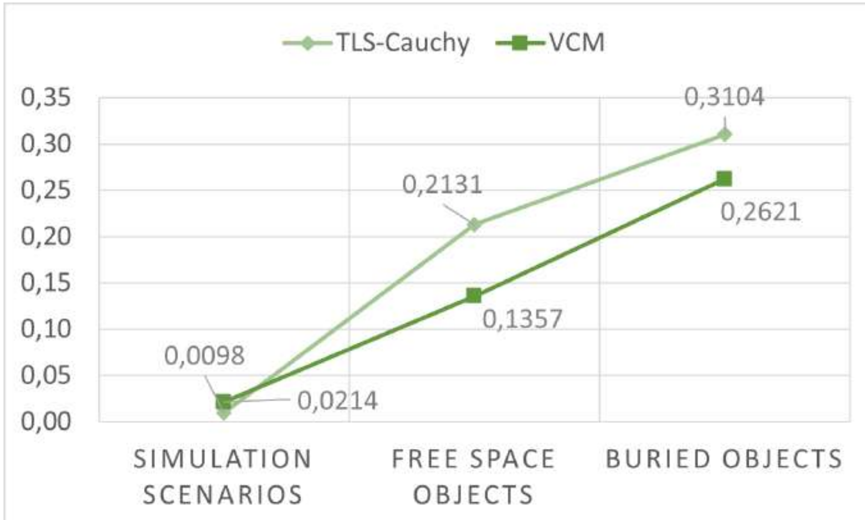

Figure **5-13**.: FSV results for both Cauchy and VCM methods, according to the comparison of the input signals and the corresponding reconstruction in simulated and experimental setups.

For the hardware suitability factor presented in Eq. 4-1, the term corresponding to A_{R^2} (from 0 to 1, being 1 a perfect reconstruction) has been changed to A_{FSV}, including an equivalence for the accuracy factor $FSVtoR = -\frac{FSV-1.6}{1.6}$. With this accomodation, the ψ_{FSV} hardware suitability factor is:

$$\psi_{FSV} = \frac{A_{FSV}}{Nt_e} = -\frac{FSV - 1.6}{1.6 \times Nt_e} \quad . \tag{5-19}$$

The result for the average VCM is then $\psi_{FSV} = 5491.2$ which is above the results for Cauchy, 558,3.

5.4. Conclusions

A new rational function approximation for the calculation of Complex Natural Resonances in radar operations, called Vector-Fitting Cauchy Method (VCM) has been presented, validated and compared to the most updated frequency domain method, Cauchy. The results are promising with a 24% percent improvement in accuracy for the 30 particular backscattering scenarios evaluated here.

VCM has an increased computational execution time (compared to Cauchy Method) using the same number of samples. This is mainly because VCM has more steps in its calculation. Nonetheless, the compuational complexity is still a linear factor of $O(m^2)$, which is directly related to the number of samples. With the average of 104 ms, VCM is still faster than time-domain CNREM, and the hardware suitability factor that includes execution time, number of samples and accuracy for the reconstruction is 5491,2, the highest for all the CNE extraction methods.

This accuracy increased was designed according to the conclusions of Chapter 4, where a frequency-domain method, being the faster and using less samples than time-domain methods, could still increase its accuracy.

As the signal becomes more complex, or less soft, VCM reduces its reconstruction accuracy, because it needs more samples and the numerical noise exponentially increases in the calculation. In this context, Cauchy is less accurate than VCM and the difference between VCM and Cauchy becomes greater or can be seen more clearly in the poles and the reconstruction in GPR operations.

VCM, compared to Cauchy, MPM and Prony methods for complex resonances calculation in radar operations is particularly, for the scenarios evaluated here, the more suitable method for a real time hardware implementation.

6. Hardware design

Based on the VCM algorithm for the extraction of CNRs designed in chapter 5, then a version of it was tested in Hardware embedded processors in order to determine the deployment state for a real-time implementation. In order to achieve this, a C code was generated for the ARM processor architecture, the result was compared to MATLAB results (to calculate numerical deviation in the results). and execution times were measured for the complete function and subfunctions also.

The ARM Cortex-A9 was selected as the target for the implementation because it is used in several embedded systems and also in Zynq platforms, where the FPGA-Processor could accelerate the performance of critical functions detected.

6.1. VCM implementation

First, an outline of the functions to be implemented in C code is describe in Fig. **6-1**. The fact that several Singular Value Decompositions of matrix of average size 33 x 33 have to be performed. For this reason, and if the computational complexity of an SVD is $\mathcal{O}(\min(mn^2, m^2n))$, or in this case $\mathcal{O}(m^2)$ with m as the number of rows and columns for the squares matrices, the computational complexity of VCM is a factor of $\mathcal{O}(m^2)$ [58].

VCM was implemented in C language in order to test its performance and compare the execution. As an example, Fig. **6-4** displays the poles for a metal cylinder calculated with MATLAB and executed in the ARM processor. There is no noticeable difference between the resonances calculated, because the 32 bit double-precision data types allow precise results.

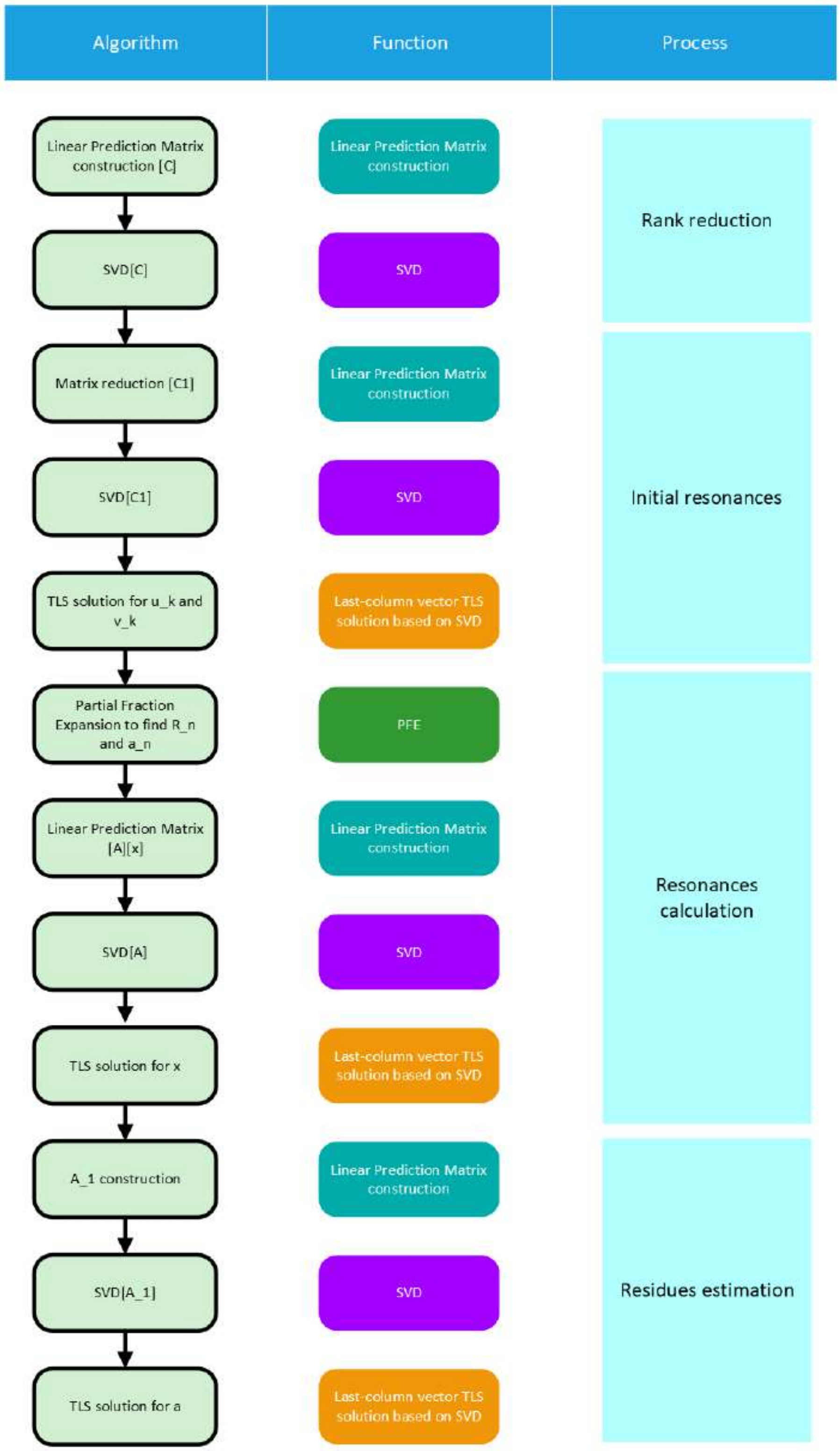

Figure **6-1**.: VCM algorithm outline, function description and overall steps to be implemented in C code.

The hardware platform is the Xilinx ZC706, showed in Fig. **6-2**, and the Processor In the Loop (PIL) process is whoed in Fig. **6-3**. The process for the comparison with Matlab and the processor results were achieved in approximately 5 minutes, in an core i7 and 32 GB Ram PC.

Figure **6-2**.: HW platform ZC706

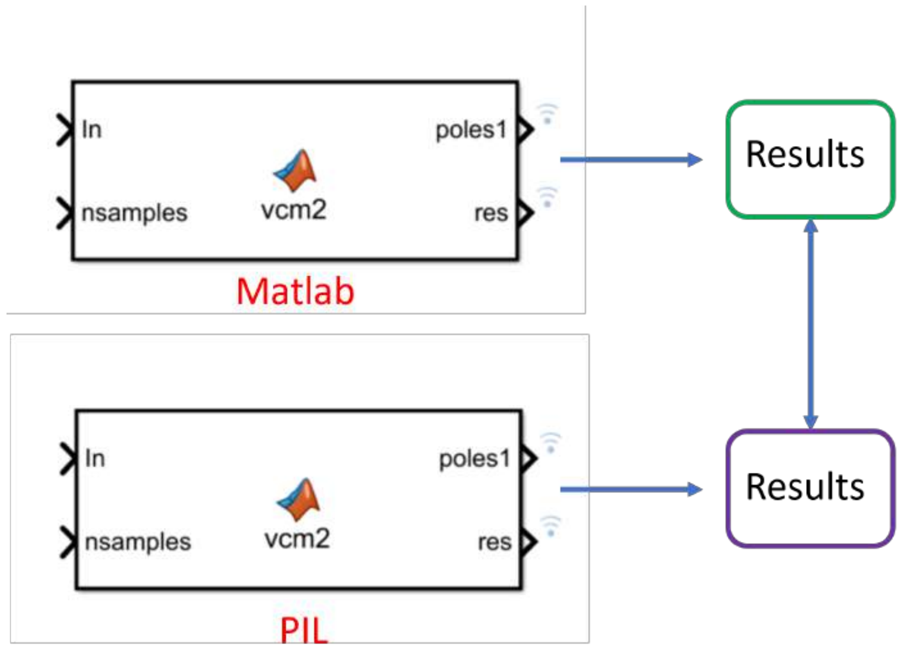

Figure **6-3**.: VCm tests for Processor in the loop for an ARM Cortex-A9 and Matlab.

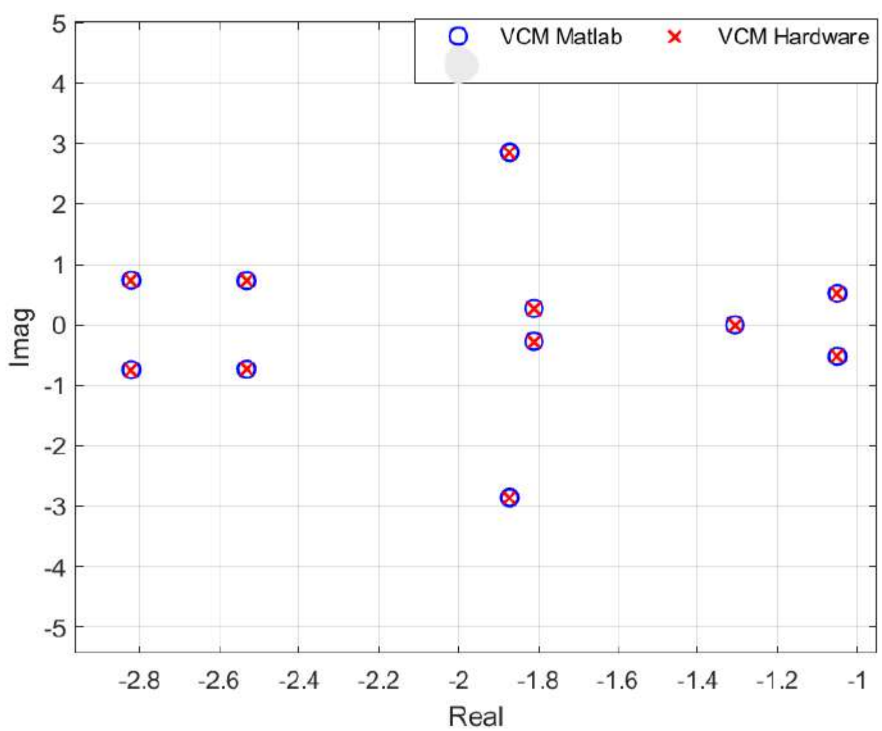

Figure **6-4**.: CNRs calculated in Matlab and in an ARM Cortex-A9 processor.

Table **6-1** shows the run results for the implementation using processor in the loop (PIL) functions in Matlab for including a hardware processor in the calculations and measure the time for every function. The number for the average execution time and the number of samples were calculated directly for the 9 backscattering signals for the corner reflector, the metal cylinder and the detonator.

As the average execution time is 1.42 seconds, it can be categorized as an operation time (demining) algorithm, and is close to a real-time implementation if the system gets a hardware acceleration through the FPGA in some of the critical functions. However, this would also increment the overall cost of the portable hardware.

VCM implementation				
Function	**Maximum execution time (ms)**	**Average execution time (ms)**	**Average number of samples**	**Input data size**
VCM	1975	1429	30	1256

Table **6-1**.: Results for hardware execution of VCM in the ARM Cortex-A9 used in ZC706 board. The input size remained the same for all the tests.

The results analysis for the time consumption for every function group is describe in Fig. **6-5**, where processes involving SVD and the TLS solution used (QR-decomposition, an SVD and the determination of the last column vector of V') are critical. Although this is a expected result, then this provides an initial insight for the critical components that could be improved to reduce the execution time in an embedded processor, or at least for a ARM Cortex-A9 based embedded system.

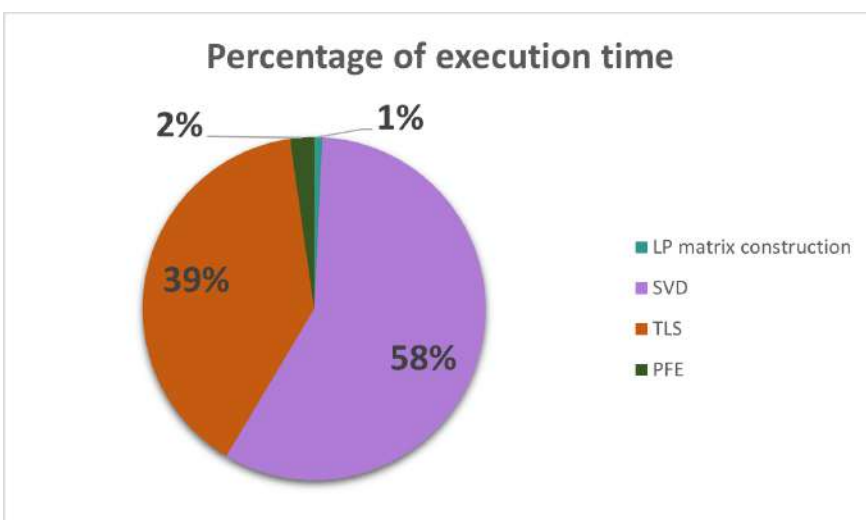

Figure **6-5**.: Percentage of execution time for every function group described for the VCM algorithm outline

6.2. Conclusions

A version of VCM was tested in an ARM Cortex-A9 processor, where the average execution time for experimental signals is 1.42 seconds. This is an acceptable time for demining operations, but could still be improved for a real time implementation in the future. For this, relying on the critical functions identified (SVD and TLS), an FPGA hardware acceleration of these functions running, for example, in the zc706 development platform will lead to real time operations.

This is the first iteration in the hardware design. This means that improving execution time has to take into account the signal acquisition subsystem and the resources it consumes from the hardware platform.

7. Conclusions and future work

In order to contribute to the Improvised Explosive Devices detection in Colombia, for a humanitarian demining process, the non-invasive Ground Penetrating Radar techniques and algorithms of the Singularity Expansion Method were automated, tested, improved and implemented in an ARM processor commonly used in embedded systems. This provides the base for a low-cost signal processing that can identify metallic objects based in the Complex Natural Resonances calculated, unique for every shape and material.

A detailed explanation of the Prony, Matrix Pencil and Cauchy methods in time and frequency domain, also with examples of the CNRs calculated and its automation was presented. The first conclusion here is that the validation of the CNR-based reconstruction of the signal through R2 coefficient or FSV is necessary as a first validation of the CNRs extraction, alongside a resonance validation through experiments. Then, the presented factor for evaluating hardware implementation suitability based on execution time, accuracy and number of samples, is used for a formal determination of comparison for an operation-time implementation in an embedded system. Time and frequency domain methods were classified and recommendations for use scenarios were given based on simulation and experimental results. Although the Cauchy method outperforms time-domain SEM methods, principal components of that algorithm that could be improved were identified and covered.

A new rational function approximation for the calculation of Complex Natural Resonances in radar operations, called Vector-Fitting Cauchy Method (VCM) has been presented, validated, compared and implemented. The results are promising with a 24 % percent improvement in accuracy and a significant improvement in the Hardware Suitability Factor. VCM compared to Cauchy, MPM and Prony methods for complex resonances calculation in radar operations is particularly, for the scenarios evaluated here, the more suitable method for a real time hardware implementation, which, for now, runs in 1.42 seconds in an embedded processor.

Beside the algorithm insights provided in this document, the applications of CNREM exceed buried IEDs detection. As the appendixes show, our work can be used to compress information, determine and interpolate the channel behavior of two antennas, and segment an input Linear Prediction Matrix for parallel process execution.

Finally, this work represents a section of a fully standalone and automated portable prototype that needs to include the signal acquisition circuit, autonomous movement, field training (probably with CNN) and a Graphic User Interface, hopefully remaining as a low-cost device for humanitarian military and civil use.

A. Folded Alias MPM

Here we proposed and evaluate a method for reducing the size of the Linear Prediction Matrix used during the Matrix Pencil Method. This proposal considers the division of a time domain signal in W frequency segments that can be processed individually and whose results can be put together in the final stage. The evaluation of the suggested approach is presented here in terms of the coefficient of determination R2 for the reconstructed signal, and focuses on either reducing the hardware requirements for back-scattering signal processing or its parallelization. The article can be found here [6].

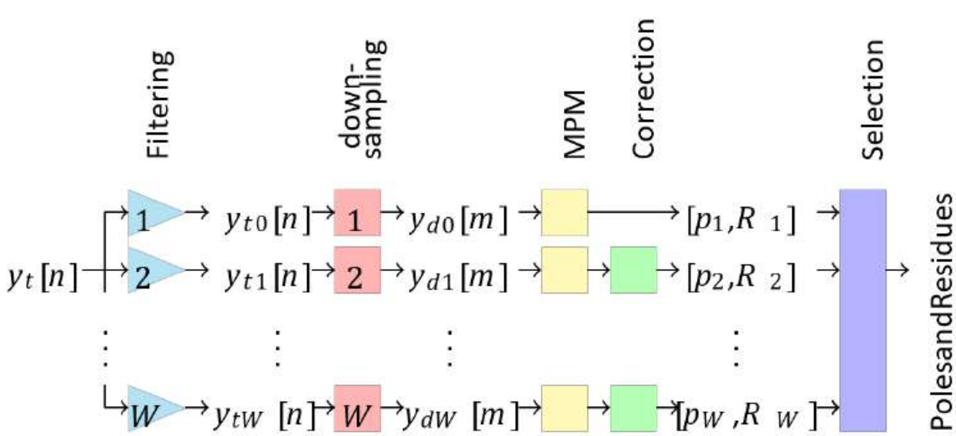

Figure **A-1**.: Folded MPM schematic [6]

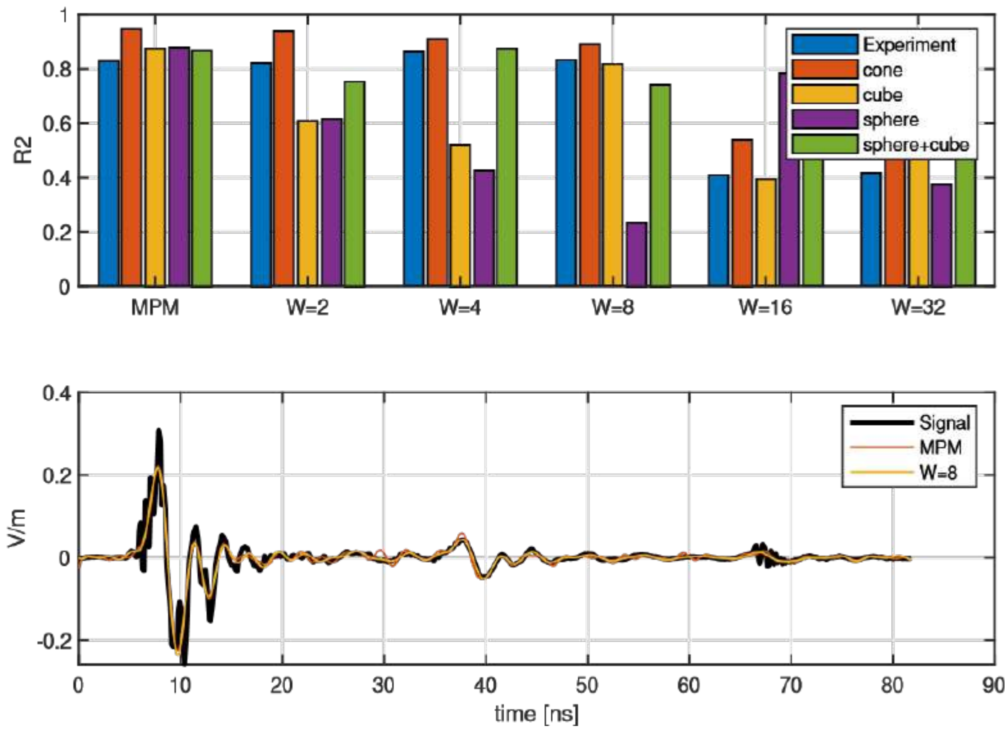

Figure **A-2**.: Coefficient of determination R2 for 5 back-scattering signal reconstructed for W = 2,4,8,16,32 and comparison between one original signal, reconstructed with original MPM and the Folded MPM proposed [6]

B. Study on data compression with SEM

Here we describe a data compression of a time-domain acoustic signal using the Matrix Pencil Method (MPM). The results show that the selection of critical parameters like time window and sampling frequency can effectively work alongside MPM, to reduce an audio signal data to a set of residues and poles, and have an accurate reconstruction of the vector related to the original audio. The papers can be found in [59] and [7].

M	*Compression percentage[%]*	*Correlation coefficient[%]*
5	99,318	89,12
10	98,63	96,89
15	97,95	98,18
20	97,27	99,13
30	95,909	89,96

Figure **B-1**.: Compression percentage of acoustic signals with Matrix Pencil Method [7]

C. Channel identification and modeling of two antennas based on SEM.

The determination of the cross-coupling between two nearby parabolic antennas was achieved through a frequency-domain CNREM, i.e. a parametric modeling of the front door coupling using Poles and Residues, extracted through the Cauchy method. The article can be found in [8].

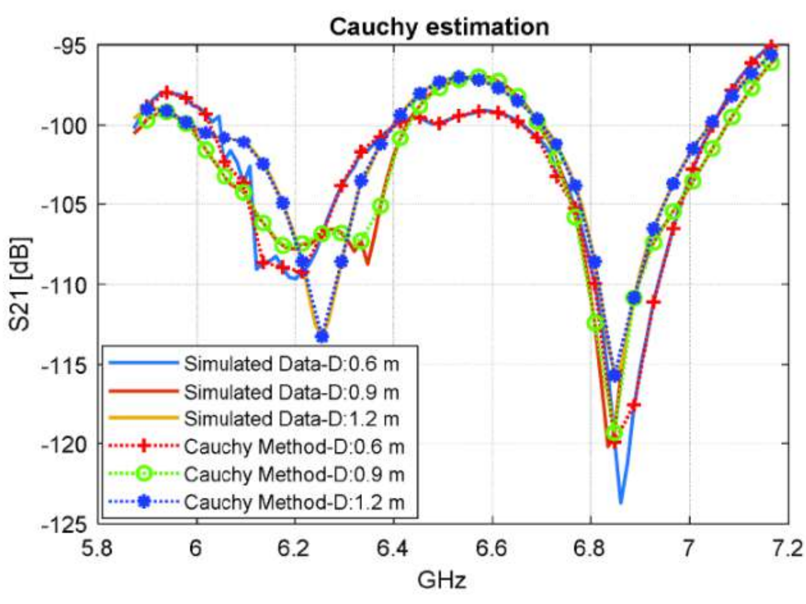

Figure **C-1**.: Coupling of two parabolic antennas separated 100 m, and the cauchy-based modeling reconstruction [8].

Bibliography

[1] H. M. Jol, *Ground penetrating radar theory and applications.* elsevier, 2008.

[2] R. Persico, *Introduction to ground penetrating radar: inverse scattering and data processing.* John Wiley & Sons, 2014.

[3] RFSpace. TSA600 Ultra-Wideband PCB Tapered Slot Antenna. (2022, Feb 23). [Online]. Available: http://rfspace.com/RFSPACE/Antennas$_f$*iles/TSA600.pdf*

[4] S. Lambot, E. C. Slob, I. van den Bosch, B. Stockbroeckx, and M. Vanclooster, "Modeling of ground-penetrating radar for accurate characterization of subsurface electric properties," *IEEE transactions on geoscience and remote sensing*, vol. 42, no. 11, pp. 2555–2568, 2004.

[5] S. A. Gutiérrez Duarte, "Application of time-frequency transformations in polarimetric ultra-wideband mimo-gpr signals for detection of colombian improvised explosive devices," *Departamento de Ingeniería Eléctrica y Electrónica*, 2019.

[6] A. Gallego, F. Roman, E. Neira, F. Vega, and C. Kasmi, "Linear prediction matrix segmentation for matrix pencil method in backscattering signal scenarios," in *2021 International Conference on Electrical, Computer and Energy Technologies (ICECET).* IEEE, 2021, pp. 1–3.

[7] D. Chaparro-Arce, A. Gallego, F. Albarracin-Vargas, C. Gutierrez, F. Vega, and C. Pedraza, "Matrix pencil method applied to the compression of audio data in naval operations," in *2020 IEEE International Conference on Computational Electromagnetics (ICCEM).* IEEE, 2020, pp. 254–256.

[8] A. Rangel, A. Gallego, F. Vega, J. Becerra, and R. Campos, "Parametric macromodeling of the coupling between two nearby parabolic antennas using the cauchy method," in *2020 IEEE International Conference on Computational Electromagnetics (ICCEM).* IEEE, 2020, pp. 64–65.

[9] C. E. Baum, A. E. Hopper, and H. N. Hambric, *Unexploded Ordnance(UXO): the problem.* SUMMA, 1999.

[10] C. N. de Memoria Histórica y Fundación Prolongar, *La guerra escondida. Minas antipersonal y remanentes de explosivos en Colombia.* Bogotá, Colombia: CNMH, 2017.

[11] "Estadísticas de asistencia integral a las víctimas de map y muse," Jan 2022. [Online]. Available: http://www.accioncontraminas.gov.co/Estadisticas/estadisticas-de-victimas

[12] K. M. Lowe, L. A. Wallis, C. Pardoe, B. Marwick, C. Clarkson, T. Manne, M. A. Smith, and R. Fullagar, "Ground-penetrating radar and burial practices in western a rnhem l and, a ustralia," *Archaeology in Oceania*, vol. 49, no. 3, pp. 148–157, 2014.

[13] A. Benedetto and S. Pensa, "Indirect diagnosis of pavement structural damages using surface gpr reflection techniques," *Journal of Applied geophysics*, vol. 62, no. 2, pp. 107–123, 2007.

[14] M. Kuloglu and C.-C. Chen, "Ground penetrating radar for tunnel detection," in *2010 IEEE International Geoscience and Remote Sensing Symposium*. IEEE, 2010, pp. 4314–4317.

[15] M. Manteghi, D. B. Cooper, and P. P. Vlachos, "Application of singularity expansion method for monitoring the deployment of arterial stents," *Microwave and Optical Technology Letters*, vol. 54, no. 10, pp. 2241–2246, 2012.

[16] T. Kelly, M. Angel, D. O'Connor, C. Huff, L. Morris, and G. Wach, "A novel approach to 3d modelling ground-penetrating radar (gpr) data – a case study of a cemetery and applications for criminal investigation," *Forensic Science International*, vol. 325, p. 110882, 2021. [Online]. Available: https://www.sciencedirect.com/science/article/pii/S0379073821002024

[17] M. Sato, J. Fujiwara, X. Feng, Z.-S. Zhou, and T. Kobayashi, "Development of a hand-held gpr md sensor system (alis)," in *Detection and Remediation Technologies for Mines and Minelike Targets X*, vol. 5794. SPIE, 2005, pp. 1000–1007.

[18] V. Kovalenko, *Advanced GPR data processing algorithms for detection of anti-personnel landmines*. TU Delft, Delft University of Technology, 2006.

[19] C. Rappaport, M. El-Shenawee, and H. Zhan, "Suppressing gpr clutter from randomly rough ground surfaces to enhance nonmetallic mine detection," *Subsurface Sensing Technologies and Applications*, vol. 4, no. 4, pp. 311–326, 2003.

[20] J. Sachs, *Handbook of ultra-wideband short-range sensing: theory, sensors, applications.* John Wiley & Sons, 2013.

[21] L. Van Kempen and H. Sahli, "Signal processing techniques for clutter parameters estimation and clutter removal in gpr data for landmine detection," in *Proceedings of the 11th IEEE Signal Processing Workshop on Statistical Signal Processing (Cat. No. 01TH8563)*. IEEE, 2001, pp. 158–161.

[22] D. Daniels, "Ground penetrating radar, ser," *IEE Radar, Sonar, Navigation and Avionics Series. London: The Institution of Electrical Engineers*, vol. 15, 2004.

[23] S. Lambot, E. Slob, I. Van Den Bosch, B. Stockbroeckx, B. Scheers, and M. Vanclooster, "Estimating soil electric properties from monostatic ground-penetrating radar signal inversion in the frequency domain," *Water Resources Research*, vol. 40, no. 4, 2004.

[24] S. Lambot, E. Slob, I. Van den Bosch, B. Stockbroeckx, B. Scheers, and M. Vanclooster, "Gpr design and modeling for identifying the shallow subsurface dielectric properties," in *Proceedings of the 2nd International Workshop onAdvanced Ground Penetrating Radar, 2003.* IEEE, 2003, pp. 130–135.

[25] A. Gallego, E. Pineda, S. Gutierrez, and F. Román, "Complex natural resonances extraction methods for ground penetrating radar operations," *Digital Signal Processing*, 2021, manuscript Under Review.

[26] E. Kennaugh and D. Moffatt, "Transient and impulse response approximations," *Proceedings of the IEEE*, vol. 53, no. 8, pp. 893–901, 1965.

[27] R. K. Mains, *Complex natural resonances of an object in detection and discrimination.* ElectroScience Laboratory, Department of Electrical Engineering, The Ohio ..., 1974, vol. 74, no. 282.

[28] C. E. Baum, "On the singularity expansion method for the solution of electromagnetic interaction problems," DTIC Document, Tech. Rep., 1971.

[29] A. Ramm, "Theoretical and practical aspects of singularity and eigenmode expansion methods," *IEEE Transactions on Antennas and Propagation*, vol. 28, no. 6, pp. 897–901, 1980.

[30] F. Tesche, "On the analysis of scattering and antenna problems using the singularity expansion technique," *IEEE Transactions on Antennas and Propagation*, vol. 21, no. 1, pp. 53–62, 1973.

[31] C. Baum, "On the use of contour integration for finding poles, zeros, saddles and other function values in the singularity expansion method," *Mathematics Notes*, 1974.

[32] J. M. Myers, S. S. Sandler, and T. T. Wu, "Electromagnetic resonances of a straight wire," *IEEE transactions on Antennas and Propagation*, vol. 59, no. 1, pp. 129–134, 2010.

[33] C. Bouwkamp, "Hallén's theory for a straight, perfectly conducting wire, used as a transmitting or receiving aerial," *Physica*, vol. 9, no. 7, pp. 609–631, 1942.

[34] C. E. Baum, "The singularity expansion method: Background and developments," *Electromagnetics*, vol. 1, no. 4, pp. 351–360, 1981.

[35] C. Baum, E. Rothwell, K.-M. Chen, and D. Nyquist, "The singularity expansion method and its application to target\nidentification," *Proceedings of the IEEE*, vol. 79, no. 10, pp. 1481–1492, 1991.

[36] C. L. Dolph, "the Singularity Expansion Method and Complex Singularities of Exterior Scalar and Vector Scattering in Acoustics & Electromagnetic Theory," p. 77, 1979.

[37] W. Lee, "Identification of a target using its natural poles using both frequency and time domain response," 2013.

[38] Y. Hua and T. K. Sarkar, "Matrix Pencil Method for Estimating Parameters of Exponentially Damped/Undamped Sinusoids in Noise," *IEEE Transactions on Acoustics, Speech, and Signal Processing*, vol. 38, no. 5, pp. 814–824, 1990.

[39] M. A. Rahman and K. B. Yu, "Total least squares approach for frequency estimation using linear prediction," *IEEE Transactions on Acoustics, Speech, and Signal Processing*, vol. 35, no. 10, pp. 1440–1454, 1987.

[40] W. Lee, T. K. Sarkar, H. Moon, and M. Salazar-Palma, "Computation of the natural poles of an object in the frequency domain using the cauchy method," *IEEE Antennas and Wireless Propagation Letters*, vol. 11, pp. 1137–1140, 2012.

[41] L. C. Chan, *Subsurface electromagnetic target characterization and identification.* The Ohio State University, 1979.

[42] J. Young, L. J. Peters, and C.-c. Chen, *Chapter 5: Characteristic resonance identification techniques for buried targets seen by Ground Penetrating Radar.* SUMMA, 1999.

[43] D. V. Giri and F. M. Tesche, "An overview of the natural frequencies of a straight wire by various methods," *IEEE Transactions on Antennas and Propagation*, vol. 60, no. 12, pp. 5859–5866, 2012.

[44] R. Prony, "Essai experimental et analytique sur les lois de la dilatabilite des fluides elastiques et sur celles de la force expansive de la vapeur de leau et de la vapeur de lalkool, r differentes temperatures," *Journal Polytechnique ou Bulletin du Travail fait r Lecole Centrale des Travaux Publics, Paris, Premier Cahier*, pp. 24–76, 1795.

[45] D. Tufts and R. Kumaresan, "Singular value decomposition and improved frequency estimation using linear prediction," *IEEE Transactions on Acoustics, Speech, and Signal Processing*, vol. 30, no. 4, pp. 671–675, 1982.

[46] J. Makhoul, "Linear Prediction: A Tutorial Review," *Proceedings of the IEEE*, vol. 63, no. 4, pp. 561–580, 1975.

[47] G. H. Golub and C. F. Van Loan, "An Analysis of the Total Least Squares Problem," pp. 883–893, 1980.

[48] T. K. Sarkar, F. Hu, Y. Hua, and M. Wicks, "A real-time signal processing technique for approximating a function by a sum of complex exponentials utilizing the matrix-pencil approach," *Digital Signal Processing*, vol. 4, no. 2, pp. 127–140, 1994.

[49] T. K. Sarkar and O. Pereira, "Using the Matrix Pencil Method to Estimate the Parameters of a Sum of Complex Exponentials," *IEEE Antennas and Propagation Magazine*, vol. 37, no. 1, pp. 48–55, 1995.

[50] A. Caboussat and G. K. Miers, "Numerical approximation of electromagnetic signals arising in the evaluation of geological formations," 2009.

[51] D. Chaparro-Arce, S. Gutierrez, A. Gallego, C. Pedraza, F. Vega, and C. Gutierrez, "Locating ships using time reversal and matrix pencil method by their underwater acoustic signals," *Sensors*, vol. 21, no. 15, p. 5065, 2021.

[52] T. Sarkar and O. Pereira, "Using the matrix pencil method to estimate the parameters of a sum of complex exponentials," *IEEE Antennas and Propagation Magazine*, vol. 37, no. 1, pp. 48–55, 1995.

[53] A.-L. Cauchy, "Sur la formule de Lagrange relative à l'interpolation," in *Cours d'analyse de l'École Royale Polytechnique:*. Cambridge: Cambridge University Press, 1821, pp. 525–529. [Online]. Available: https://www.cambridge.org/core/books/cours-danalyse-de-lecole-royale-polytechnique/sur-la-formule-de-lagrange-relative-a-linterpolation/BBE87600C81E0072348EA4676F1551CE

[54] J. Yang and T. K. Sarkar, "Interpolation/extrapolation of radar cross-section (RCS) data in the frequency domain using the cauchy method," *IEEE Transactions on Antennas and Propagation*, vol. 55, no. 10, pp. 2844–2851, 2007.

[55] A. Gallego, F. Vega, and A. Rangel, "Hybrid method for the estimation of complex natural resonances using cauchy and vector fitting," in *2020 IEEE International Conference on Computational Electromagnetics (ICCEM)*. IEEE, 2020, pp. 69–71.

[56] A. P. Duffy, A. J. Martin, A. Orlandi, G. Antonini, T. M. Benson, and M. S. Woolfson, "Feature selective validation (fsv) for validation of computational electromagnetics (cem). part i-the fsv method," *IEEE transactions on electromagnetic compatibility*, vol. 48, no. 3, pp. 449–459, 2006.

[57] B. Gustavsen and A. Semlyen, "Rational approximation of frequency domain responses by vector fitting," *IEEE Transactions on power delivery*, vol. 14, no. 3, pp. 1052–1061, 1999.

[58] P. A. Businger and G. H. Golub, "Algorithm 358: singular value decomposition of a complex matrix [f1, 4, 5]," *Communications of the ACM*, vol. 12, no. 10, pp. 564–565, 1969.

[59] D. Chaparro-Arce, S. Gutierrez, A. Gallego, C. Pedraza, F. Vega, and C. Gutierrez, "Locating ships using time reversal and matrix pencil method by their underwater acoustic signals," *Sensors*, vol. 21, no. 15, p. 5065, 2021.